2015

Evaluation Of Magnesium-Based Alloys As Degradable Biomaterials

Nan Zhao
North Carolina Agricultural and Technical State University

Evaluation of Magnesium-based Alloys as Degradable Biomaterials

Nan Zhao

North Carolina A&T State University

A thesis submitted to the graduate faculty

in partial fulfillment of the requirements for the degree of

MASTER OF SCIENCE

Department: Chemical, Biological and Bio Engineering

Major: Bioengineering

Major Professor: Dr. Donghui Zhu

Greensboro, North Carolina

2015

The Graduate School

North Carolina Agricultural and Technical State University
This is to certify that the Master's Thesis of

Nan Zhao

has met the thesis requirements of
North Carolina Agricultural and Technical State University

Greensboro, North Carolina
2015

Approved by:

Dr. Donghui Zhu
Major Professor

Dr. Jenora T. Waterman
Committee Member

Dr. Boyce Collins
Committee Member

Dr. Matthew B.A. McCullough
Committee Member

Dr. Stephen Knisley
Committee Member

Dr. Stephen Knisley
Department Chair

Dr. Sanjiv Sarin
Dean, The Graduate School

Biographical Sketch

Nan Zhao was born on July 7th in Xi'an, Shaanxi, China. He received his Bachelor of Science in bioengineering from Northwest Agricultural & Forest University in 2012. He is a candidate for the Master of Science degree in Bioengineering at North Carolina A&T State University. He has served as a Graduate Research Assistant in the NSF-Engineering Research Center for Revolutionizing Metallic biomaterials at North Carolina A&T State University.

Acknowledgements

I would like to acknowledge my advisor Dr. Donghui Zhu who believed in me enough to select me to be a part of his research team. His instruction and encouragement is always pushing me to keep improving. I would like to thank Dr. Jagannathan Sankar for providing funding for my graduate study; Dr. Jenora T. Waterman for letting me work in her lab; Dr. Zhigang Xu for providing the novel materials used for experiments and use of his lab equipment; Dr. Leon White for assistance on the electrochemical corrosion tests; Mr. Benjamin Workman for help with magnesium coating and cell culture; and Mr. Paul McGhee for assistance on sample surface roughness measurement. I also want to thank Dr. Boyce Collins, Dr. Jenora T. Waterman, Dr. Stephen Knisley, and Dr. Matthew B.A. McCullough for serving on my thesis committee.

Table of Contents

List of Figures

List of Tables

Abstract

Biomaterials including ceramic material, polymer material, metallic material and composite material have been used in biomedical scaffolds, artificial tissues, and drug delivery systems for a long time. Magnesium (Mg) and Mg-based alloys are a new generation of degradable metallic materials that have attracted great attention in the last ten years. The advantages of Mg alloys as biomaterials are their good biocompatibility and biodegradability. Mg as an essential element in human body is an enzyme cofactor for over 300 biochemical reactions. However, the degradation process of Mg material may hinder the potential application. The purpose of this study is to evaluate the biocompatibility of pure Mg and Mg alloys by different *in vitro* methods. We believe that Mg material could be used as vascular stent material and bone orthopedic implant materials.

The effect of different metals used in Mg stent materials on endothelial cells, biocompatibility of Mg-Rare Earth (RE) alloys, collagen self-assembly on Mg bone orthopedic material, and endothelialization on hydrofluoric acid conversion coating were studied. Scanning electron microscope, electrochemical corrosion test, hemolysis test, platelet adhesion test, cell viability test, cell proliferation test, immunostaining and q-PCR were used. Major results include: (i) the effect of Mg on endothelial cell viability and proliferation is dose-dependent; (ii) alloying with rare earth elements could improve endothelial cell attachment and viability; (iii) the structure of collagen self-assembly on Mg material is affected by collagen monomer concentration, assembly time, pH, and degradation products; and (iv) hydrofluoric acid conversion coating can improve endothelial cell attachment and proliferation. This study successfully shows that Mg alloys have the potential to be medical implant materials.

CHAPTER 1

Introduction

1.1 Biomaterials

A biomaterial is any substance, natural or man-made, that is used to help the biological system to fulfill its function or to induce the system to recover from certain defects. Since the late 18th century, biomaterials have been used in joint replacements, bone plates, bone cement, artificial ligaments, artificial tendons, dental implants, blood vessel prostheses, heart valves, cardiovascular stent, and artificial skin [1,2]. There are three development stages for biomaterials: inert biomaterial, resorbable biomaterial, and regenerative biomaterial [3]. For inert biomaterial, its function is mainly to maintain local system integrity and there is limited tissue response. Resorbable biomaterials can be degraded and absorbed by local tissues over a certain amount of time. Regenerative biomaterial should not only have the basic characteristics of a biomaterial but also be able to induce and promote the self-healing of the tissue. Based on the material composition, the most common classes of biomaterials include ceramic material, polymer material, metallic material, and composite material.

Polymer biomaterial has some unique properties such as flexibility, preferable biocompatibility, light weight and an adjustable range of physical and mechanical properties. Polymer materials can be divided into two categories based on their origin: artificial polymer and native polymer. Polytetrafluoroethylene (PTFE), Dacron (PET) and polyglycolic acid (PGA) are the most commonly used synthetic materials in vascular grafts [4-6]. Among them, synthetic poly (ethylene terephthalate) (Dacron) and expanded polytetrafluoroethylene (ePTFE) have been successfully used for reconstruction of peripheral arteries in large diameter vascular grafts. Besides vascular graft, polymer materials are also used in artificial skin, artificial heart valve,

vascular stent and drug delivery system. Generally, ceramic biomaterial and metal biomaterial are often chosen for hard tissue applications because of their relative higher mechanical strength compared with polymer biomaterials. On the other hand, polymer has better biocompatibility compared with metal and ceramic materials.

Ceramic biomaterials are also called bioceramics. Common ceramic biomaterials include aluminia, zirconia, and bioglass. The major characteristics of ceramic biomaterials are high hardness, brittleness, and high corrosion resistance. Ceramic biomaterials have been used in several different biomedical applications such as dentistry, orthopedics as well as medical sensors.

Metallic biomaterial usually has very strong mechanical strength. Titanium, titanium alloys, stainless steel, nitinol, and cobalt alloys are called permanent metallic materials due to the fact that their corrosion rate in physiological conditions is very slow. Biodegradable metallic materials are a new generation of metallic biomaterials which can be degraded and absorbed by the host. In many cases, biomaterials or medical implants do not need to be present after the local tissue has healed. Therefore, another surgery is needed to remove the medical devices made by permanent materials. Degradable metallic materials can avoid another surgery to remove the medical devices. Iron, zinc, zinc alloys, magnesium (Mg), and Mg alloys are currently extensively researched for degradable biomaterials.

1.2 Mg and Mg Alloys

Mg is a very attractive biodegradable material which has very good biocompatibility and low thrombogenicity [7]. Mg also is an essential element in human body required for many biological/metabolic activities. In addition, Mg ion is the cofactor for many enzymes and pure Mg can be easily degraded in simulated body fluid and lose the mechanical strength. The

degradation products of Mg alloys may include metal ions, metal particles, and hydrogen gas, which all might hamper the biocompatibility of Mg materials. Mg alloyed with Al, Zn, Ca, Zirconium (Zr), Yttrium (Y), and rare earth elements (REs) can significantly improve the corrosion resistance and mechanical strength. Mg and its alloys are often used for vascular stent and bone orthopedic application [8].

1.3 Mg Stent

Vascular system disease including cardiovascular disease, cerebrovascular disease, and peripheral arterial disease is the leading cause of mortality in the United States. Currently about 30% of global death is caused by cardiovascular disease [9]. Cardiovascular stents have been used to treat vascular stenosis for a long time. Dozens of biomaterials have been tried to demonstrate their ability as a suitable candidate for the stent material, such as stainless steel, nitinol, cobalt alloys, titanium alloys, Mg-based alloys and polymers. Enough mechanical strength until tissue heals, high corrosion resistance and good biocompatibility are the three major requirements for a suitable stent material. The key advantage of Mg-based material over others for stent material is its potential to reduce or even eliminate the late restenosis which occurs very frequently in permanent stent materials. Despite the advantages of Mg-based stent, high corrosion rate and low mechanical strength are two major limitations for stent application. Alloying with other metal elements and surface coating are used to conquer the two problems. The first biodegradable metallic stent was based on Mg by Armco Iron and implanted in an animal model in 2001 [10]. Figure 1 shows a vascular stent based on Mg alloy [11]. Endothelialization is a key factor for successfully stent implantation. Therefore, it is very important to study how Mg and Mg degradation products interact with vascular endothelial cells.

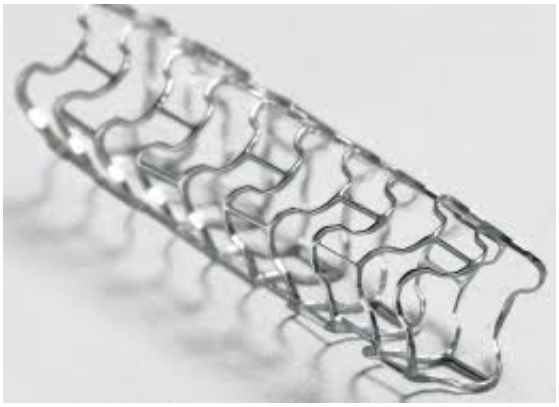

Figure 1. Mg based cardiovascular stent [11].

1.4 Mg for Orthopedic Application

Metallic biomaterials play an important role in repairing or replacement of diseased or damaged bone tissues because of their suitability for load-bearing. There are several advantages of Mg-based alloys for bone orthopedic application over other metal biomaterials, e.g., stainless steel, titanium alloys, and cobalt-chromium alloys. First, their physical and mechanical properties including density (1.74-2.0 g/cm^3), elastic modulus (41-45 GPa), and compressive yield strength (65-100 MPa), are much closer to that of natural bone, and therefore can avoid the stress shielding effect [12-14]. Table 1 summarizes the physical and mechanical properties of some implant materials with comparison to natural bone [15]. Second, Mg is an essential element for many biological activities including enzymatic reaction, formation of apatite, and bone cells adsorption [16]. Third, Mg alloys can eliminate the necessity of a second surgery to remove the permanent bone implants. A lot of studies have shown that Mg implant materials had better bone cell induction compared with other biomaterials [15,17-19]. However, how Mg material interacts with extracellular matrix (ECM) in bone tissues is still unknown. ECM plays an important role in the structure and function of bone tissues. Therefore, it is very important to study how Mg materials affect the ECM structure and their functions.

Table 1

Summary of the physical and mechanical properties of some orthopedic biomaterials with comparison to natural bone [15]

Properties	Natural bone	Mg	Ti alloy	Co–Cr alloy	Stainless steel
Density (g/cm^3)	1.8–2.1	1.74–2.0	4.4–4.5	8.3–9.2	7.9–8.1
Elastic modulus (Gpa)	3–20	41–45	110–117	230	189–205
Compressive yield strength (Mpa)	130–180	65–100	758-1117	450–1000	170–310
Fracture toughness (MPam$^{1/2}$)	3–6	15–40	55–115	N/A	50–200

1.5 Thesis Outline

Chapter 2 will be a literature review of current research focus of Mg and Mg-based biomaterials, popular methods used for assessing the biocompatibility, potential applications for tested materials, and coating materials for Mg. Chapter 3 will discuss methods and materials used to evaluate the toxicity of Mg degradation products, biocompatibility of Mg materials, and coatings for Mg. Chapter 4 will discuss all results regarding the material characterization, biocompatibility of the materials, and surface coating. Lastly, chapter 5 presents a summary of the results discovered and suggested future studies.

CHAPTER 2

Literature Review

The history of application Mg as a degradable biomaterial dates back to late 19th century. Lambotte reported the first use of Mg as a plate to secure a fracture involving the bones of the lower leg [20]. Due to the fast corrosion rate of pure Mg *in vivo*, the trial failed only 8 days after the surgery. In 1944, Troitskii and Tsitrin reported a study where Mg alloying with cadmium was fabricated into plates and screws and used to secure bone fractures [21]: 25 of 34 cases were successfully implanted and no inflammatory reaction or high serum magnesium level was observed. In 1986, Richard Jorgensen filed a patent on a Mg device for haemostatic clip; he found that Mg clips and staples were safer for closing vessels in brain or deep wounds [22]. Later in the 20th century, Mg was researched as biodegradable cardiovascular stent and orthopedic biomaterials. During the recent 10 years, there is a boom of study of Mg-based alloys.

2.1 Alloying Elements.

Pure Mg has very fast degradation rate and lower mechanical strength. Those two properties can be improved by alloying with other metal elements. Al, Zn, Ca, Mn, Zr, Y and rare earth elements (REs) are the most common elements used in Mg alloys. Table 2 summarized the composition of some commercially available Mg alloys and alloys that were widely studied recently. The mechanical properties and corrosion resistance could be improved by aluminum significantly [23]. However, excessive aluminum ions have a high toxic effect on nervous system [24]. Zn a nd Ca are two common necessary elements in human body and it is believed that Zn is one effective element for improving the mechanical strength of Mg-based alloy [25]. In addition, Zn and Mn can also enhance the corrosion resistance by avoiding the galvanic corrosion caused by nickel and iron impurities [25].

Table 2

Composition of different Mg-based alloys

Alloy	Elements Percentage (wt%)								Reference
	Mg	Al	Zn	Ca	Mn	Zr	Re	Other	
WE43	Balance	/	0.2	/	0.13	0.36	3.8	Y:4.16	[26]
AZ31	Bal	2.83	0.8	/	0.37	/	/	Si:0.1~0.05	[27,28]
ZW21	Bal	/	2	0.25	0.15	/	/	Y:1	[29]
AZ31B	Bal	1.2	0.74	/	0.35	/		Si:0.026	[30]
AZ63	Bal	5.6	2.7	0.2	0.18~0.5	/	/	Cu:0.2	[31]
AZ91D	Bal	8.5	0.6	/	0.25	/	/	Cu:0.25	[32]
Mg-Sr	Bal	0.007~0.012	/	/	0.003	/	/	Sr:0.3~2.5	[33]
Mg-Mn-Zn	Bal	<0.3	1.05~3.05		1.08~1.11	/	/	/	[25]
Mg-Zn-Ca	Bal	/	30~25	4~5	/	/	/	/	[34]
Mg-Li-Al-Re	Bal	2-4	/	/	/	/	2	Li:3.5~8.5	[35]
Mg-Nd-Zn-Zr	Bal	/	0.164	/	0.003	0.413	3.13	/	[36]
Mg-Nd-Zn-Zr	Bal	/	0.22	/	/	/	3.53	/	[37]
Mg-Zn-Y-Nd	Bal	/	2	/	/	/	0.5	Y:0.46	[38]
Mg-Al-Ca-Mn	Bal	3.5	/	3.3	0.4	/	/	/	[39]

One of the most attractive approaches today in fabricating new Mg-based alloy is to add rare earth elements (Sc, Y, and all lanthanides) to the alloy system [40]. On the other hand, their toxicity is still controversial and remains as a main concern. Nd, Gd, Y, and Er are the most commonly used REs. Besides WE43, AZ31 and other commercial Mg alloys, the mechanical strength, corrosion behavior and biocompatibility of Mg-Y, Mg-Nd-Y, Mg-Zn-Y, Mg-Zn-Y-Nd,

Mg-Nd-Zr, Mg-Nd-Zn-Zr were extensively investigated [37,41-45]. Seitz et al. tested cell viability and cell proliferation after exposure to the Mg-Nd degradation solution, and their results indicated that alloying with Nd did not affect the cell viability [46]. Murine aneuploid fibrosarcoma cell line(L-929) cells cultured with extracts from Mg-1.5Y-1.2Zn-0.44Zr showed that there was improved cell proliferation with no significant cytotoxicity [47]. In vitro cell culture with rare earth chlorides showed that most rare earth elements have obvious effect on viability of human umbilical cord perivascular cell at concentrations over 1000 μg/mol [48]. However, it is still unclear whether REs released from stent will affect the endothelialization process.

2.2 Material Preparation and Characterization.

The grain sizes of the alloys, second-phase distribution, mechanical properties as well as absence of structural defects are strongly related to the processing routes. Pure Mg and other alloying elements are typically melted and cast under an inert environment. As-casted alloys often have an inhomogeneous grain structure, which results in lower mechanical strength and fast corrosion at the grain boundary. Zhang et al. estimated the effects of extrusion and heat treatment on the Mg-based alloy system [36]. It was shown that extrusion can significantly improve the mechanical properties of the alloy by grain refinement and precipitation strengthening. In addition, the mechanical properties decreased as the increase of the extruded temperature (250-450ºC). It was also shown that cyclic extrusion compression could optimize the microstructure and corrosion behavior of Mg–Zn-Y-Nd alloy compared with as-cast and extrusion alloys [49]. After extrusion of ZM21 alloy, the grain size was within submicrometer range and the hardness was significantly higher than that of the coarse-grained ZM21 alloy [50].

Annealing can significantly improve the elongation of Mg-Zn-Y alloy, but the yield strength ofthe alloys with different contents decreases [51].

Table 3

Mechanical properties of Mg alloys

Alloy name	Fabrication	Grain size(middle linear length um)	Yield strength(MPa)	UTS (Mpa)	Elongation (%)	Reference
Pure Mg	As-rolled	/	113	170	12	[31]
WE43	As-extruded	10~30	216.67	297.67	21.67	[52]
AZ31B	As-extruded	/	200	255	12	[53]
AZ91D	Die-cast	250	70.67	170.74	4.3	[52]
ZM21	As-extruded	0.52~15	180~340	259~353	/	[50]
Mg-Sr	As-casted	5~30	/	210~240	/	[54]
Mg-Li	As-extruded		~70	101~148	75~190	[35]
Mg-Zn-Ca	As-casted	/	/	162	/	[55]
Mg-Zn-Y	As-extruded	3~4	160	270	20	[56]
Mg-Li-Al	As-extruded		~90	~148	~220	[35]
Mg-Mn-Zn	As-extruded	4~9	246	280	20	[25]
Mg-Li-Al-Re	As-extruded	/	73~130	200~230	15~46	[35]
Mg-Nd-Zn-Zr	As-extruded	/	124~189	226~243	17~26	[36]
Mg-Zn-Y-Nd	As-casted	/	105	209	10.6	[49]
Mg-Zn-Y-Nd	As-extruded	5~15	185	316	15.6	[49]
Mg-Al-Ca-Mn	As-extruded	/	/	420	5.6	[39]

Mechanical properties are always the top priority when a new alloy is evaluated as stent material. Yield strength, ultimate tensile strength and elongation are the three most common factors to determine if the material could fulfill its function with respect to a mechanical perspective. In addition, for most balloon expandable stents, 20% to 30% elongation is needed for the stent expansion process. Table 3 summarizes the mechanical strength of some Mg alloys.

Immersion test, electrochemical corrosion test, and in vitro cell culture were often used to determine the corrosion property and biocompatibility. Immersion test in solution can provide a simplified model about how stent materials degrade in a static solution. Table 4 summarizes the immersion corrosion parameters of different alloys. Sample size and corrosion solution in different experiments varied, which could have direct effects on the corrosion rate. It is the same scenario for electrochemical corrosion tests (Table 5). Electrochemical impedance spectroscopy and potentiodynamic polarization showed dominant role in revealing Mg-alloy galvanic corrosion.

Table 4

Immersion degradation test of Mg material

Alloy name	Size/mm	solution	Duration/ d	Corrosion rate ($mg/d*cm^2$)	Reference
WE43	D=8,T=1.5	SBF,APS	5,10	0.363	[26,37]
ZW21	D=17.5,T=3.6	SBF	7	/	[29]
MgSr	H=40,W=20,T =6	Hank's	1~3	2~23	[33]
MgLi	D=10,T=2	Hank's	3~10	/	[35]
MgLiAl	D=10,T=2	Hank's	3~10	/	[35]
MgMnZn	D=11.3,T=2	SBF	3~30	/	[25]
MgLiAlRe	D=10,T=2	Hank's	3~10	/	[35]
MgNdZnZr	D=12,T=5	SBF	10	0.09~0.14	[36]
MgNdZnZr	D=12,T=5	APS	10	0.337mm/y	[57]
MgZnYNd	D=8,T=5	SBF	5	4.8~8.04	[49]
MgZn	D=11.3	0.9%NaCl	3~6	1.5~3.9	[58]

2.3 Surface Modification.

The most effective way to improve the corrosion resistance and biocompatibility of stent materials without compromising their mechanical strength is surface modification. Surface treatment and surface coating are the two common strategies. The difference between them is that surface treatment does not add any distinctive layer of substance and it only modifies the

composition or microstructure of the outer layer. Some of the techniques that have been commonly used for stent surface modification include galvanization, sputtering followed by ion bombardment, pulsed biased arc ion plating, micro-arc oxidation, dipping, spraying, and plasma-based deposition [59-66].

Table 5

Electrochemical corrosion tests of Mg alloys

Alloy name	Shape	Area(cm^2)	Solution	I_{corr}(mA/cm^2)	E_{corr}(V)	Degradation rate(mm/y)	Reference
Pure Mg	Square	1	Hanks	0.0598	-1.554		[31]
AZ31	Round	0.785	PBS	0.182	-1.54	/	[67]
AZ31B	/	/	SBF	0.0013	-1.69	/	[30]
WE43	Round	1	SBF	0.509	-1.85	/	[26]
MgLiAlRe	Round	0.785	Hank's	0.418~1.412	-1.482~-1.587	0.1~3.4	[35]
MgZnCa	Square	1	SBF	0.11	-1.645	/	[55]
Mg-0.5Sr	/	0.72	Hank's	0.005	-1.58	0.2~0.4	[33]
MgZnYNd	Round	1	SBF	1.08	-1.7	/	[38]
MgNdZnZr	Round	1	APS	0.00141	-1.69	/	[57]
MgZnY	/	1	SBF	0.44	-1.792	/	[56]
MgLi	Round	0.785	Hank's	0.428~0.461	-1.52~-1.565	0.1~0.16	[35]
MgLiAl	Round	0.785	Hank's	-1.587	0.418	0.1	[35]

Mg alloy coated with PLGA by dipping method was tested by Li et al. [58]; their immersion and potentiodynamic tests showed that coating with PLGA can significantly reduce the corrosion rate. Besides, osteoblast cells demonstrated good morphology and spread well on the coated Mg samples. In contrast, there was no cell attachment observed on the bare Mg surface. In another study, PLA and PCL layer of 15 to 20 μm were coated on the high purity Mg surface [68]. PLA and PCL coated Mg had higher free corrosion potentials and smaller corrosion currents. In addition, the weight loss and surface characterization showed that the interaction

between polymer and the Mg surface may undermine the corrosion resistance of coated high purity Mg. Moreover, adhesion of pyrrole to the AZ31 surface could reduce the corrosion potential and corrosion current, indicating good corrosion resistance compared with bare AZ31. Wang et al. compared the poly(1,3-trimethylene carbonate) (PMTC) and PCL as coating materials on the Mg-Mn-Zn alloy surface [69]. The static and dynamic hemocompatibility test showed that platelets, red blood cells and leukocytes attached on the PMTC coated Mg were much less than that on the 316 stainless steel, PCL coated and bare Mg. Electrochemical corrosion test, dynamic degradation test and in vivo degradation test all demonstrated that the PMTC coated Mg had higher biocompatibility.

Table 6

Effect of some coatings on the corrosion of Mg alloys

Alloy	Material	E_{corr}(V, uncoated)	E_{coor}(V,coated)	Icorr (uA/cm^2,uncoated)	Icorr (uA/cm^2,coated)	Reference
AZ31	Fluoride	-1.57	-1.54	1820	209	[71]
WE43	Phytic acid	-1.85	-2.80~-1.79	509	3070~508	[26]
WE43	SiC	4.9	0.6	/	/	[26]
AZ91D	Ceramic	-1.75	-1.61~-1.39	37.1	0. 08	[72]
Mg-Zn-Ca	Hydroxyapatite	-1.645	-1.414	110	25	[55]
Mg-Zn-Y-Nd	Ti-O	-1.70	-1.65	1080	48	[38]
Mg-Zn	PLGA	-1.46	-1.44~-1.36	26.5	0.085	[58]
AZ91D	Zr power	-1.584	-1.422	607900	200.4	[73]
AZ91E	Gold	~-1.72	~-1.31	~91	~82	[74]
MgZnMn	PTMC	-1.694	-1.478	190546	15.1	[69]
MgZnMn	PCL	-1.694	-1.604	190546	1625.5	[69]
MgNdZnZr	Hydrofluoric acid	-1.69	-1.59	1.41	1.05	[57]

Xiao et al. coated the die-cast AZ60 with calcium phosphate [70]. The uncoated and coated alloys were implanted into rabbit femora. The mean weight loss of coated and uncoated alloy was 0.12 g and 0.21 g at one month respectively. CT data showed that the in vivo

degradation rate of the uncoated alloy is almost 3 times as high as that of the coated alloy. Wang et al. treated the AZ31 surface with hydrofluoric acid and sulfuric acid to form a superhydrophobic layer [67]. The corrosion current of the AZ31 coated with hydrophobic layer is a tenth of that of the bare AZ31. Superhydrophobic surfaces had less platelets adhesion after incubated with blood for 1 h. Yang et al. immersed the AZ31B in fluoric acid of 50wt% from 3 to 168 h [30]. A compact film with several irregularly distributed pores was observed on the surface of alloys. Besides, as the immersion time increases, the corrosion resistance of the treated sample also increases. Other coating materials in recent studies were summarized in Table 6.

2.4 Preclinical and Clinical Evaluation of Mg Materials.

In vitro biocompatibility tests include direct cell culturing on the Mg material surface, cell viability test, cell proliferation test, hemolysis test and platelet adhesion test. Those tests can provide data to evaluate the potential for further in vivo and clinical tests. 3-(4, 5-dimethylthiazol-2-yl)-2, 5-diphenyltetrazolium bromide (MTT) test has been the most commonly used method to test cell viability in characterizing the cytocompatibility of Mg alloys. This test is based on the detection of NAD(P)H-dependent cellular oxidoreductase enzymes. Other methods to test the cytocompatibility include MTT, Lactose dehydrogenase (LDH), Bromodeoxyuridine (BrdU), and adenosine triphosphate (ATP)-based tests [75,76]. Hemolysis test and platelet adhesion test are usually used to test the hemocompatibility of the material. Table 7 shows the effect of different alloys on cell viability and hemolysis. Animal models including dog, rabbit and pig models were used for preclinical test (Table 8). For example, sirolimus-eluting stent made from AZ31B was tested in the infrarenal abdominal aorta of rabbit [79]. Radiographs showed that most of the stent struts remain complete after 30 days implantation but fully

degraded after 120 days, suggesting that the corrosion resistance of Mg stent still needs to be improved.

Table 7

In vitro biocompatibility test of Mg alloys

Alloy	Cell viability(indirect)				Hemolysis	Reference
	Cell line	Duration(d)-viability(%)				
WE43	L929	1- ~28	2- ~32	4- ~32	9.27	[26]
WE43	L929	1-83	3-69	5-67	4.9	[26]
Mg-3.5Li	VSMC	1-130	3- ~80	5- ~80	2.6~3.75	[35]
Mg-3.5Li	ECV304	1-	3-	5-	2.6~3.75	[35]
Coated-WE43	L929	1-83	2-87	4-96	3.57	[77]
MgZnCa	L929,MG63	1-83	3-52	5-52	/	[34]
MgMnZn	/	/	/	/	0.48	[25]
MgLiAl	VSMC	1- ~182	3- ~98	5- ~90	3.75	[35]
MgLiAl	ECV304	1- ~92	3- ~75	5- ~87	3.75	[35]
MgY	VSMC	2-92	4-120	7-89	5	[31]
MgZn	L929	2-~97	4-~96	7-~96	/	[78]
Mg-0.5Sr	HUVEC	1-75	4-102	7-112	/	[33]
Mg-8.5Li-Al-Re	VSMC	1- ~105	3- ~75	5- ~60	6	[35]
Mg-8.5Li-Al-Re	ECV304	1- ~42	3- ~48	5- ~69	6	[35]
MgNdZnZr	Endothelia cell	1- 95.4	3-102.2	5- ~120	52	[57]

PROGRESS-AMS was the first clinical trial of absorbable Mg metal alloy stents where 63 patients received the stent implants [80,81]. The length and diameter of the stents ranged from 10-15 mm and 3-3.5mm. After implantation, the patient follow-up was scheduled at 4, 6, and 12 months. Coronary angiography and intravascular ultrasound showed that the lumen loss at 4 months was 0.83 mm. Mg was replaced by calcium and phosphorous compound within 2 months. A continuation of such clinical trial was published later where the long-term effects of Mg stent in human body was evaluated by angiogram and IVUS [82]. Eight patients who were in good condition after 4 months implantation were selected in this study. The net volume

obstruction was about 11% (1.3-18.2 mm^3) after 12 months implantation and the stent volume reduced from 124.5 mm^3 to 94.2 mm^3.

Table 8

Animal models used for in vivo evaluation of Mg alloys

Alloy	Stent(mm)			Animal	Position	Duration(d)	Reference
	Length	Diameter	Strut thickness				
WE43	10	2.4	0.27	dog	Femoral artery	21	[33]
WE43	10	1.2	0.15~0.2	pig	Coronary artery	10-56	[83]
AZ31B	15	3	0.155	rabbit	Infrarenal abdnominal aorta	30-120	[84]
Mg-0.5Sr	10	2.4	0.27	dog	Femoral artery	21	[33]
AZ31B	15	3	0.155	rabbit	Carotid artery	30~120	[79]
AE21	10	2	0.12-0.2	pig	Anterior,circumflex and coronary artery	10~56	[85]

The first-in-man trial of the drug-eluting absorbable metal stent based on Mg alloy was reported recently [86-88]. The stent used in this clinical trial was balloon-expandable, paclitaxel-eluting delivery system based Mg alloy. The study was carried out in 5 clinical centers including 47 patients and the clinical follow-up for the patients was arranged at 1, 6, 12, 24, and 36 months respectively. All the stents were successfully delivered to the location of lesion and the clinical follow-up ratio at 1 month, 6 months, 12 months are 100%, 100%, and 93%, respectively [87]. Except for one patient who died from non-cardiac cause and for 2 patients who withdrew their informed consents, data was collected from the rest of the patients. The luminal cross-section area loss at 6 and 12 months are 1.12 and 1.30 mm^2. This study first demonstrated the feasibility of application of Mg-based biodegradable stents in clinical treatment.

CHAPTER 3

Methodology

3.1 Material Preparation

3.1.1 Mg alloy. Mg based alloys of MgYZr-1RE, MgZnYZr-1RE (RE includes Gd and Dy, denoted as R1 and R2, thereafter), as well as MgZnCaY-*x*RE (*x*=1 and 2, RE includes Nd and Gd, denoted as R3 and R4, thereafter) were prepared by melting 99.97 % Mg ingot (Alfa Aesar, US), 99.9 % Zn, Ca granules (Sigma-Aldrich, US) and Mg-30RE master alloys in an electrical resistance furnace (Mbraun, US) under the protection of argon gas. Mg-30RE is a gift from Institute of Metal Research, Chinese Academy of Science. The alloy fabrication process was carried out by Dr.Zhigang Xu [89].

All the materials were then cut (Techcut 5, Allied High Tech Products, US) into 10×10×1 mm square and polished (EcoMet 250 Grinder, Buehler, US) with SiC paper up to 1200 grit. All samples were supersonically cleaned (M2510 Ultrasonic cleaner, Branson, US) in absolute acetone and ethanol (Sigma-Aldrich, US). For hemocompatibility and endothelialization tests, each side of the samples was sterilized by UV light (1380 Biological Safety Cabinet, Thermo, US) exposure for 30 min. At least 3 replicates were used in each experiment ($n \geq 3$).

3.1.2 Mg extracts solution. Mg extracts were prepared according to ISO 10993-12 [90]. Samples were soaked with serum free endothelial culture media (ECM, ScienCell, USA) as the extraction medium with a ratio of 1.25 ml/cm^2 in a humidified atmosphere with 5 % CO_2 at 37 °C for 3 days. The supernatant was removed, filtered by a double layer 0.8 μm filter (BD Biosciences, US) and refrigerated at 4 °C.

3.1.3 Ion stock solutions. The chlorides of Sodium (Na), Mg, Ca, Zn, Al, Y, Dy, Nd, and Gd (>99.99 %, Sigma Aldrich, USA) were dissolved into deionized water at concentration of 1

M (Na, Mg, Ca) and 0.01 M (The rest). The stock solutions were filtered, and stored at 4℃. Final ion solutions were made by mixing stock solution with ECM.

3.2 Mg Material Characterization

3.2.1 Electrochemical corrosion. Potentiodynamic polarization curves were measured by Gamry instruments (Gamry Ref 600, Gamry Instruments, US) using a three-electrode cell as described previously [30]. The reference electrode, counter electrode and working electrode were saturated calomel, platinum and testing materials. Tests were carried out in Hank's balanced solution (HBS, Invitrogen, US) after samples were immersed for a while. All the DC polarization data was fitted and analyzed by Echem Analyst 6.0 (Gamry instrument, US). The corrosion rate of all the samples were calculated according to ASTM-G102-89 [91].

3.3 *In Vitro* Biocompatibility

3.3.1 Hemolysis. Fresh human whole blood with sodium citrate was purchased from Cedarlane Labs (Cedarlane, US). The test was performed according to the method described previously [28]. In brief, 0.2 ml diluted human whole blood (4:5) was added to 10 ml centrifuge tubes after all the samples were pre-soaked into 10 ml Dulbecco's Phosphate Buffered Saline (DPBS, Invitrogen, US) for 1 hour. The positive and negative groups were diluted blood with 10 ml deionized water and diluted blood with 10 ml DPBS, respectively. Then all the samples were incubated at 37 ℃ for 1 hour. After centrifuge (Biofuge Stratos, Thermo, US) at 800 g for 5 min, the supernatants were collected and the absorbance (A) was measured using a UV-Vis Spectrometer (Thermo, US) at 545 nm. The hemolysis rate (HR) was calculated by the following equation:

① $HR = [A(sample) - A(negative)]/[A(positive) - A(negative)]$.

3.3.2 Platelet adhesion. Platelet rich plasma (PRP) with platelets of 10^8/ml (All Cells, US) was used for platelet adhesion test. All the samples were pre-soaked in DPBS for 1 hour. Then 100 µl PRP was overlaid on the surface of each sample and incubated (Heracell 150 I, Thermo, US) at 37 °C for 1 hour. Samples were gently rinsed by DPBS for 3 times to remove the non-adherent platelets. After that, 4 % paraformaldehyde (Boston Bioproducts, US) was used to fix the adherent platelets followed by ethanol gradient (50 %, 60 %, 70 %, 80 %, 90 %, and 100 %) dehydration for 10 minutes. All the samples were coated by gold nanoparticle for 2 min and observed by SEM (SU8000, Hitachi, US). The number of adherent platelets was counted by Image-Pro Plus 6.0 (Media Cybernetics, US) on at least four different SEM images for each sample.

3.3.3 Indirect cytocompatibility. Human aorta endothelial cells (HAEC) were purchased from Sciencell Research Laboratories (California, US). HAECs were expanded ECM with 10 % fetal bovine serum (Sciencell, US), 100 U/ml penicillin (Sciencell, US) and 100 µg/ml streptomycin (Sciencell, US) on the fibronectin coated 75-flasks (BD Biosciences, US) at 37 ºC in humidified incubator with 5 % CO_2 and the passages 4-5 were used. Indirect MTT (Invitrogen, US) test was used to measure cell toxicity. HAECs were seeded in the 96-well cell culture plate (BD Bioscience, US) for 24 hours to allow cell attachment. ECM then was replaced by 100 µl 10 %, 25 %, 50 %, and 75 % extract solutions. The positive control and negative control were serum free ECM and serum free ECM with 10 % DMSO (Invitrogen, US), respectively. After incubating in the humidified incubator for 2, 4, and 7 days, MTT test was performed according to the manufacturer's protocol. The absorbance (A) was measured at 570 nm by a Microplate reader (SpectraMax, Molecular Devices, US). Morphology of cells was

characterized by Digital Inverted Microscope (EVOS, Advanced Microscopy, US). Cell viability was calculated by the following equation:

② $Viability = (A_{sample}-A_{negative})/(A_{positive}-A_{negative})$

3.3.4 *In vitro* direct endothelialization. Mg alloy samples were soaked into serum free ECM for 3 days in 24-well culture plate (BD Bioscience, US) before using. Cell suspension (100 µl) with density of 100,000 cell/100 µl was overlaid on the surface of samples. Fibronectin coated tissue culture plates were used as a control group. Cells were allowed to settle for 30 min in an incubator with 5 % CO_2 at 37ºC. DPBS was used to gently wash the sample surface for 3 times to remove the unattached cells. And then 2 ml serum free ECM was added to each well. After 3 hours and 24 hours, Mg samples were transferred to another new plate and cells on the sample surface were characterized by LIVE/DEAD Viability Kit (Invitrogen, US) according to the manufacturer's protocol. Images were taken by Digital Inverted Microscope (EVOS, US).

3.3.5 Effect of metal ions on cell viability. HCAECs were seeded in the 96-well cell culture plate (BD Biosciences, USA) with 5,000 cells/well for 24 hours to allow cell attachment. ECM was replaced by ECM supplemented with different ion solutions and incubated for 24 hours. ECM with 10% DMSO (Life Technologies, USA) and ECM alone were positive and negative controls. Another blank reference containing same concentrate of ion solution without cells was used to exclude the interference of the ions. MTT test was performed according to the manufacturer's protocol. Absorbance (A) was measured at 570 nm by a microplate reader (SpectraMax5, Molecular Devices, USA). Cell viability was calculated by the following equation (except for the Calcium group in which A_{blank} was not deducted):

③ Viability = $(A_{sample}-A_{negative}-A_{blank})/(A_{positive}-A_{negative})$

3.3.6 Lactate dehydrogenase release. HCAECs were seeded in 96-well cell culture plate at 5,000 cells/well and incubated for 24 h. Then ECM was replaced by ECM supplemented with different ion solution. After 24 h incubation, 100 μl culture media from each well was transferred to a new plate for lactate dehydrogenase (LDH, Roche Applied Science, USA) test. Absorbance was measured by a Microplate Reader (BioTek, USA) at 490 nm. Positive control and negative control were cells cultured with ECM supplemented with 2.5% dimethylsulfoxide (DMSO, Life Technologies, USA) and ECM, respectively. LDH release was calculated by the following equation:

④ $LDH = (A_{sample}-A_{negative})/(A_{positive}-A_{negative})$

3.3.7 Cell proliferation. BrdU cell proliferation kit (Cell Signaling, USA) was used for cell proliferation test. HCAECs were seeded in 96-well cell culture plate at 5,000 cells/well. After 24 hours, ECM was replaced by different ion solutions and incubated for 24 hours. The ion concentration was set up to the concentration at which cell viability was not significantly affected. Proliferation test was performed according to the manufacturer's protocol. Absorbance was measured at 450 nm. Positive control and negative control were ECM without ion supplement and ECM without cells. Proliferation rate was calculated as following equation:

⑤ $Proliferation = (A_{sample}-A_{negative})/(A_{positive}-A_{negative})$

3.3.8 Cell migration. HCAECs ($2.5*10^5$ cells/well) were seeded in 12-well cell culture plate (BD Biosciences, USA). A straight line in cell monolayer was created by scratching the surface with a p200 pipette tip (Thermo Scientific, USA). Debris was removed by gently washing for 3 times with DPBS and cells were incubated with 3 ml ECM supplemented with different ion solutions. At 0, 6, and 24 hours, optical images were taken by Phase Contrast Microscope (Advanced Microscopy, USA). The width of the line at upper, middle and bottom

positions was measured in Image-Pro Plus 6.0 (Media Cybernetics, USA). Recovery rate (RR) and recovery speed (RS) were calculated by following equations (n=18):

⑥ RR = (Initial Gap Width – Current gap width)/Initial Gap width

⑦ RS = RR/Time

3.3.9 Cytoskeleton staining. HCAECs ($2.5*10^5$ cells/well) were seeded in 12-well cell culture plate and treated with ECM supplemented with different $MgCl_2$ for 24 hours. Image-iT Fix-Perm kit (Invitrogen, USA) was used to fix cells. Microfilament/F-actin was stained by Actin Green 488 Ready Probes Reagent (Invitrogen, USA). Microtubule was stained by mouse anti-β tubulin (Invitrogen, USA) followed by Alexa Fluor 546 rabbit anti-mouse IgG (Invitrogen, USA). Cell nucleus was stained by SlowFade Gold Anti-fade Reagent with DAPI (Invitrogen, USA). Images were taken by EVOS Inverted Fluorescent Microscope (Advanced Microscopy, USA). Fluorescent intensity of the cells was extracted by using ImageJ 1.49 software (NIH, USA). Contrast of the representative images was auto-adjusted by Image-Pro Plus 6.0.

3.3.10 Gene expression. HCAECs (10^7 cells/dish) were seeded in 100 mm culture dishes (BD Technologies, USA) and allowed to attach for 24 h. Then the cells were treated with either ECM, ECM supplemented with 10 mM $MgCl_2$, or ECM supplemented with 50 mM $MgCl_2$, respectively for 24 h. Cells were harvested and total RNA was extracted by using RNeasy Mini Kit (Qiagen, USA) and subsequently quantified by a spectrophotometer (Nanodrop 2000, USA) with OD_{260}/OD_{280} ratios between 1.9 and 2.1. Total of 600 ng RNA was used for reverse transcription by a RT^2 First Strand Kit (Qiagen, USA). Reverse-transcription was performed in a thermo cycler (T100, Bio-Rad, USA). Then 91 µl RNase-free water was added to the 20 µl cDNA mix and stored at -20℃ Freezer (Puffer Bubbard, Thermo Scientific, USA). HCAECs gene expression analysis was performed in CFX96 Touch RT-PCR Detection System (Bio-Rad,

USA) by using RT^2 Profiler PCR array (Qiagen, USA) for endothelial cell (EC). The array includes 84 functional genes, 5 housekeeping genes, 3 reverse-transcription controls (RTC), and 3 positive PCR controls (PPC). 25 µl PCR components mix including cDNA, SYBR Green Mastermix and RNase-free water was dispensed to the RT^2 Profiler PCR Array plate. After initial heat activation (95℃，10 min), cDNA was amplified as the following parameters: 95°C for 15 s and 60°C for 1 min. After the amplification, melting curve analysis was performed using the default melting curve program. Only the genes with one single melting peak were chose for final analysis. Data was analyzed by Bio-Rad CFX Manager 3.1 (Biorad, USA). $2^{-\Delta\Delta Ct}$ method was used to calculate gene fold changes [92].

3.4 Collagen Self-assembly on Mg

3.4.1 Concentration. Rat tail type I collagen solution (Life Technologies, USA) of 3 mg/ml was diluted by D-phosphate-buffered solution (DPBS, Invitrogen, USA) to 10, 50, 100, and 200 µg/ml. 50 µl final collagen solutions (*p*H of 7) were spread on testing materials surface (polished up to 1200 grit SiC paper) followed by incubating under 37℃ for 2 hours and then dehydrate with ethanol gradient. The morphology of final collagen structure was characterized by Scanning Electron Microscope (SEM, SU8000, Hitachi, USA).

3.4.2 *p*H. The *p*H of DPBS (7.49) solutions were adjusted to 7, 9, and 11 by 1 M NaOH (Sigma-Aldrich, USA) and 1 M HCl (Sigma-Aldrich, USA). Stock collagen solution was diluted by DPBS solutions with different *p*H to final concentration of 200 µg/ml. 50 µl final collagen solutions were spread on Mg and AZ31 surface (polished up to 1200 grit SiC paper) for 2 hours of assembly, then followed by dehydration using ethanol gradient. The morphology of collagen was imaged by SEM.

3.4.3 Assembly time. DPBS diluted collagen solution (50µl of 200µg/ml , *p*H of 7) was spread on Mg and AZ31 surface (polished up to 1200 grit SiC paper) and allowed to assemble for 4 h and 8 h. Then samples were dehydrated with ethanol gradient. The morphology of collagen was imaged by SEM.

3.4.4 Surface roughness. Mg and AZ31 were divided into 3 groups and polished up to 180, 800 and 1,200 grit SiC paper. Materials polished up to 180 grit SiC paper were denoted as rough surface (RS); materials polished up to 800 grit SiC paper were denoted as semi-rough surface (SR); and materials polished up to 1,200 grit SiC paper were denoted as smooth surface (SS). Surface roughness was characterized by WYKO Optical Profiler (Veeco, USA). 50µl 200µg/ml DPBS diluted collagen solution (*p*H of 7) was spread on Mg and AZ31 surface and allowed to assemble for 2 h. The morphology of collagen fibril was imaged by SEM.

3.4.5 Collagen dynamic adsorption. RS, SR and SS materials were soaked into 1 ml 60 µg/ml diluted collagen solution (*p*H of 7) with only one side exposed to the solution. The amount of absorbed collagen was quantified by Sirius Red Assay (Abacam, USA) according the method described previously with minor modification [93,94]. In brief, materials were soaked into collagen solution for 0.5h, 1h, 2h, 4h, and 8h, respectively. At each time point, samples were removed and washed with DPBS for 3 times. Then the unattached collagen in solution was transferred to a new tube followed by incubation with Sirius Red for 1 hour. The solutions were centrifuged at 8,000 g for 15 min and the dye was eluted by 0.1 M NaOH. The absorbance was measured at 540 nm by 10S UV-Vis Spectrometer (Thermo, USA). Standard curve of a series of collagen solution (7.5, 15, 22.5, 30, 37.5, 45, 52.5, and 60 µg/ml) was obtained as the same procedures. Linear regression was performed in Prism 5 (GraphPad, USA). The attached

collagen was calculated by subtraction of initial collagen by the collagen remained in the solution.

3.4.6 Cell attachment. Mouse osteoblasts (MC 3T3, ATCC, USA) were expanded in Minimum Essential Medium α (MEM, Life Technologies, USA) supplemented with 10 % fetal bovine serum (Sciencell, USA), 100 U/ml penicillin (Sciencell, USA) and 100 µg/ml streptomycin (Sciencell, USA) in humidified incubator (Heracell 150 I, Thermo, USA) with 5 % CO_2 as previously described [95]. Collagen solution (50 µl 200 µg/ml , *p*H of 7) was allowed to self-assemble on Mg and AZ31 with RS, SR, and SS for 2 h in a 24-well culture plate (BD Bioscience, USA). Then these materials were gently rinsed by DPBS for 3 times. 50 µl cell solution with density of 10,000 cell/ml was dipped onto the surface of collagen treated materials. Cells were allowed to attach for 30 min and then samples were washed gently with DPBS for 3 times. After 4 hours, cells were fixed with 4 % paraformaldehyde (Boston Bioproducts, USA) followed by ethanol gradient dehydration for 10 minutes. Samples were coated with gold nanoparticles for 2 min, and imaged by SEM.

3.4.7 Cell proliferation. Mg and AZ31 with different surface roughness treated by collagen as described above were used to test cell proliferation. MC 3T3 Cells were seeded onto the collagen coated material surface with density of 10,000 cell/ml in a 24-well culture plate. At 1st, 4th, and 7th day, cell culture media were changed and cells were stained by Live/Dead kit (Invitrogen, USA). Culture media were centrifuged (Biofuge Stratos, Thermo, USA) at 8,000 g for 10 min and *p*H was measured by a *p*H meter (Eutech, USA). The fluorescent images were taken by a digital inverted light microscope (EVOS, Advanced Microscopy, USA).

3.4.8 Mg^{2+} concentration. Mg^{2+} concentration was measured by xylidyl blue magnesium kit (Pointe Scientific, USA) as previously described [96]. In brief, 10 µl aliquot of test solution

was added to 1.5 ml final xylidyl solution (0.1 mM xylidyl blue, 0.13 mM EGTA, 1.4 M DMSO, 0.02 % potassium cyanide) and incubated for 10 min at room temperature. The absorbance of the mixtures was measured at 520 nm by a UV-Vis Spectrometer (Thermo, USA). Standard curve was obtained by using gradient $MgCl_2$ solution. Linear regression was performed in Prism 5 (GraphPad, USA). Mg^{2+} concentration was determined by the standard curve.

3.5 Mg Coating

3.5.1 Fluoride Coating. The prepared Mg samples were immersed horizontally in 1.0 ml of 47-51 % hydrofluoric acid (Sigma-Aldrich, US) for 3 days. At day 3, the alloys were removed from hydrofluoric acid (HF) and allowed to air dry. The SU8000 SEM (Hitachi, US) was used to measure the surface morphologies of the alloys, and the Quantax EDS for SEM (Bruker, US) was used to measure the alloys' thicknesses.

3.5.2 Collagen coating. Rat tail type I collagen (3 mg/ml) was obtained from life technologies, US. The stock collagen solution was diluted with DPBS (Invitrogen, US) to the final concentration of 200 μg/ml, and then placed onto the prepared material surfaces. Following surface coating, the alloys were incubated in a humidified incubator (Heracell 150 I, Thermo, US) at 37.0 ºC with 5.0 % CO_2 for two hours. After two hours, samples were washed with DPBS for 3 times to remove unattached collagen followed by gradient ethanol dehydration. All the materials were stored at 4 ºC.

3.5.3. *In vitro* endothelialization. A total of 50 μl endothelial cell (50,000 cells/mL) with serum free culture medium were pipetted onto the surface of each sample in a 24-well tissue culture plate (BD Biosciences, US). Thereafter, the cells were allowed to attach for fifteen minutes. Then all the materials were gently washed with DPBS for 3 times to remove the unattached cells. Thereafter, each alloy was immersed in 2.0 ml serum free culture medium, and

the HCAECs were incubated in a humidified environment at 37.0 ºC, 5.0 % CO_2. LIVE/DEAD Viability Kit (Invitrogen, US) was used to test cell attachment and viability at 1, 2, and 3 days, respectively. Culture medium was changed every 24 hours. Culture medium was removed from the wells, and the materials were incubated for 30 minutes with 1.0 ml DPBS containing 20 µM Ethidium Homodimer-1 and 5 µM Calcein AM. Following incubation, cells were imaged under digital inverted light microscope (EVOS, Advanced Microscopy, US).

3.6 Statistical Analysis

All data was expressed as Mean±SD. Statistical analysis was performed in Prism 5 software (GraphPad, US). For analysis of ion dose effects, nonlinear fit for dose-response-inhibition in Prisma was used. Unpaired student's t-test was performed to compare the significance level of treatment group with control group. One-way ANOVA was used to test significant difference in hemolysis and cell viability. Multiple comparisons within one group were performed by using one-way ANOVA followed by post hoc analysis. It is considered significantly different statistically if the $P < 0.05$.

CHAPTER 4

Results

4.1 Endothelial Responses Exposed to Metal Ions.

4.1.1 EC viability. ECs were treated with different ion solutions for 24 hours and the relative MTT viability results are shown in *Figure 2*. The dashed lines indicate the half maximal effective concentration (EC50). Stars indicate that the cell viability was significantly decreased compared to control (n=3, $P<0.05$).

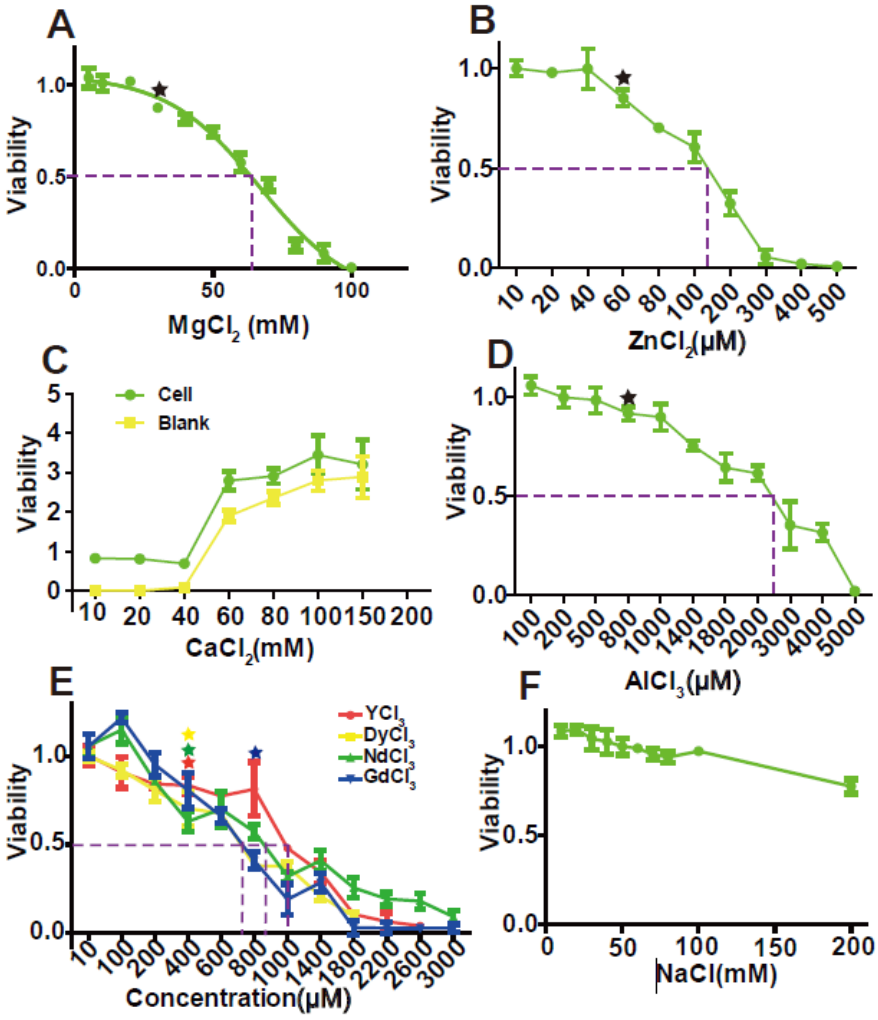

Figure 2. MTT viability of ECs as a function of salt concentration.

The overall cell viability decreased as ion concentrations increased except for the group treated with $CaCl_2$. For the group of NaCl treatment, viability was not affected up to 100 mM and then decreased to 80.03±0.2% at 200 mM (*Figure 2*F).With the increase of Mg ion concentration from 8 mM to 103 mM, viability decreased from 105% to almost 0. Nonlinear fit (R^2=0.97) for dose-response-inhibition showed that viability was not significantly affected when the Mg^{2+} is less than 30 mM. The half maximal effective concentrations (EC50) for $MgCl_2$, $ZnCl_2$, and $AlCl_3$ were about 66.7 mM, 130 µM and 2,400 µM, respectively. The EC50 for the four REs ranges from 710 to 990 µm. When the $CaCl_2$ concentration was higher than ~60 mM, it could interfere with the MTT result (*Figure 2*C).

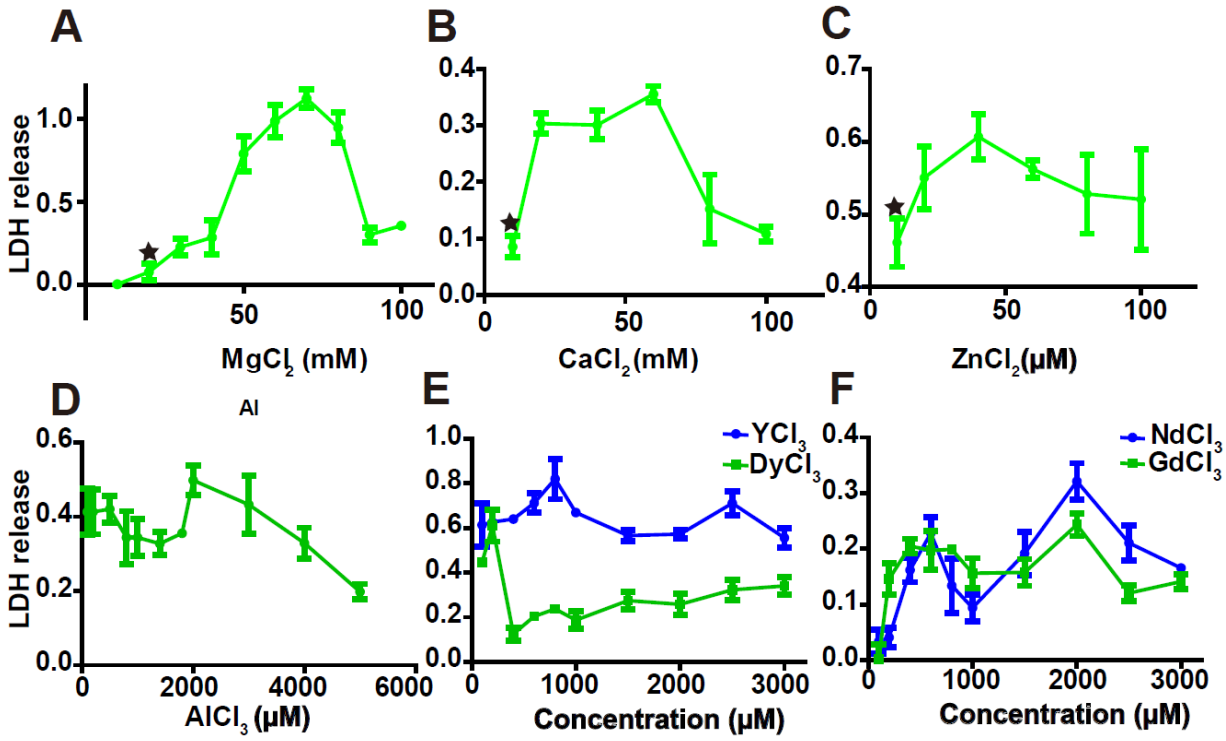

Figure 3. LDH release from ECs as a function of salt concentration.

4.1.2 Lactate dehydrogenase (LDH) release. The relative amount of LDH released into cell culture media after endothelial cells treated with $MgCl_2$, $CaCl_2$, $ZnCl_2$ $AlCl_3$ and REs was

shown in *Figure 3*. Stars indicate that the LDH release was significantly increased compared to control (n=3, $P<0.05$). As the concentration of $MgCl_2$ increased from 10 mM to 70 mM, the relative quantity of released LDH increased from 0.6±0.4% to 112.4±5.6%, and then started to drop. The highest LDH release in $CaCl_2$ treated group was at concentration of 60 mM. In the $ZnCl_2$ treated group, LDH release showed the same tendency and the turning point was around 40 μM of $ZnCl_2$. LDH release decreased first when concentrations of $AlCl_3$ increased from 100 to 1,800 μM, then it increased again and peaked at 2,000 μM $AlCl_3$ and then started to drop (*Figure 3*D). In the REs treated groups, the overall LDH release increased with increasing ion concentrations (*Figure 3*E and *Figure 3*F).

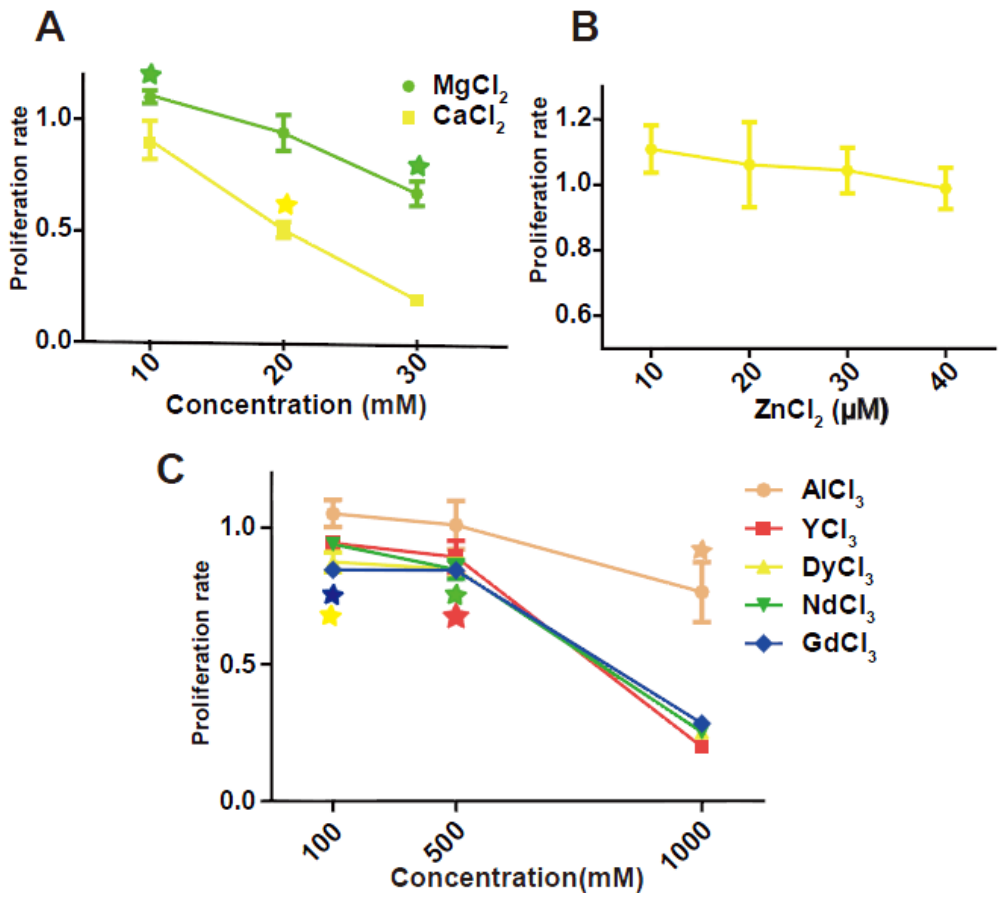

Figure 4. ECs proliferation rate as a function of salt concentration.

4.1.3 EC proliferation rate. The overall HCAECs proliferation rate decreased as the concentrations of $MgCl_2$ and $CaCl_2$ increased (*Figure 4*). One interesting observation was that $MgCl_2$ at 10 mM improved the proliferation rate to 114±0.70%, significantly higher than control group, while the proliferation rate of 10 mM $CaCl_2$ treated group was 90.5±14.9% which is not significantly different from the control. The proliferation rate of cells treated with 10 μM $ZnCl_2$ increased to 110.8±12.5%, and then decreased slowly as the increase of $ZnCl_2$ to 40 μM (*Figure 4*B). For $AlCl_3$, cell proliferation was significantly decreased at 1,000 μM. REs had much severe adverse effects on the cell proliferation compared with $AlCl_3$. $DyCl_3$ and $GdCl_3$ significantly decreased the proliferation rate at 100 μM. In all REs treated HCAECs, cell proliferation declined gently with concentrations increase from 100 to 500 μM, and then decreased sharply from 500 to 1,000 μM.

4.1.4 EC migration. *Figure 5* shows the EC migration test. ECs were treated with endothelial cell culture media supplemented with different concentration of magnesium chloride. The gap width (GW) of the line was calculated by Image Pro software. Recovery rate (RR) and recovery speed (RS) are shown on the top left corner of the image. For the control group, the recovery ratio (RR) was 39±4% after 6 h and the wound completely healed after 24 h. For the group supplemented with 10 mM and 20 mM $MgCl_2$, the simulated wound also completely healed after 24 h. The RSs and RRs were even significantly higher than that of control group during the first 6 h ($n=18$, $P<0.05$). In the 30 mM and 40 mM groups, RR and RS were comparable to the control group at 6 h while significantly decreased at 24 h. In the 50 mM group, not only the RR and RS significantly decreased at 6 h, but also a large amount of cells peeled off along the edge of the wound.

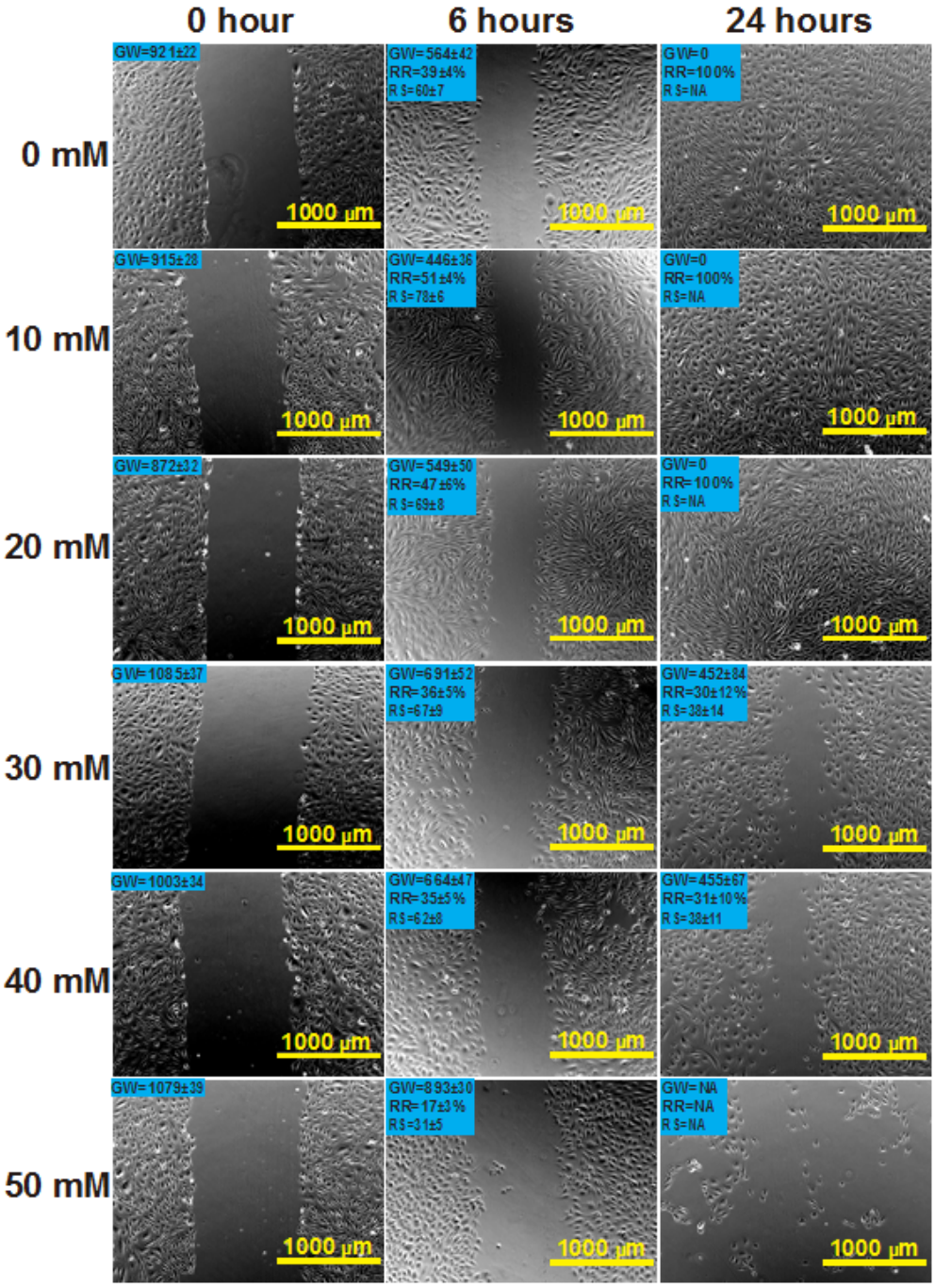

Figure 5. Optical images of ECs migration under the effect of $MgCl_2$.

4.1.5 Cytoskeleton staining. Cytoskeleton proteins, actin (Green) and microtubule (Red) structures were shown in *Figure 6*.

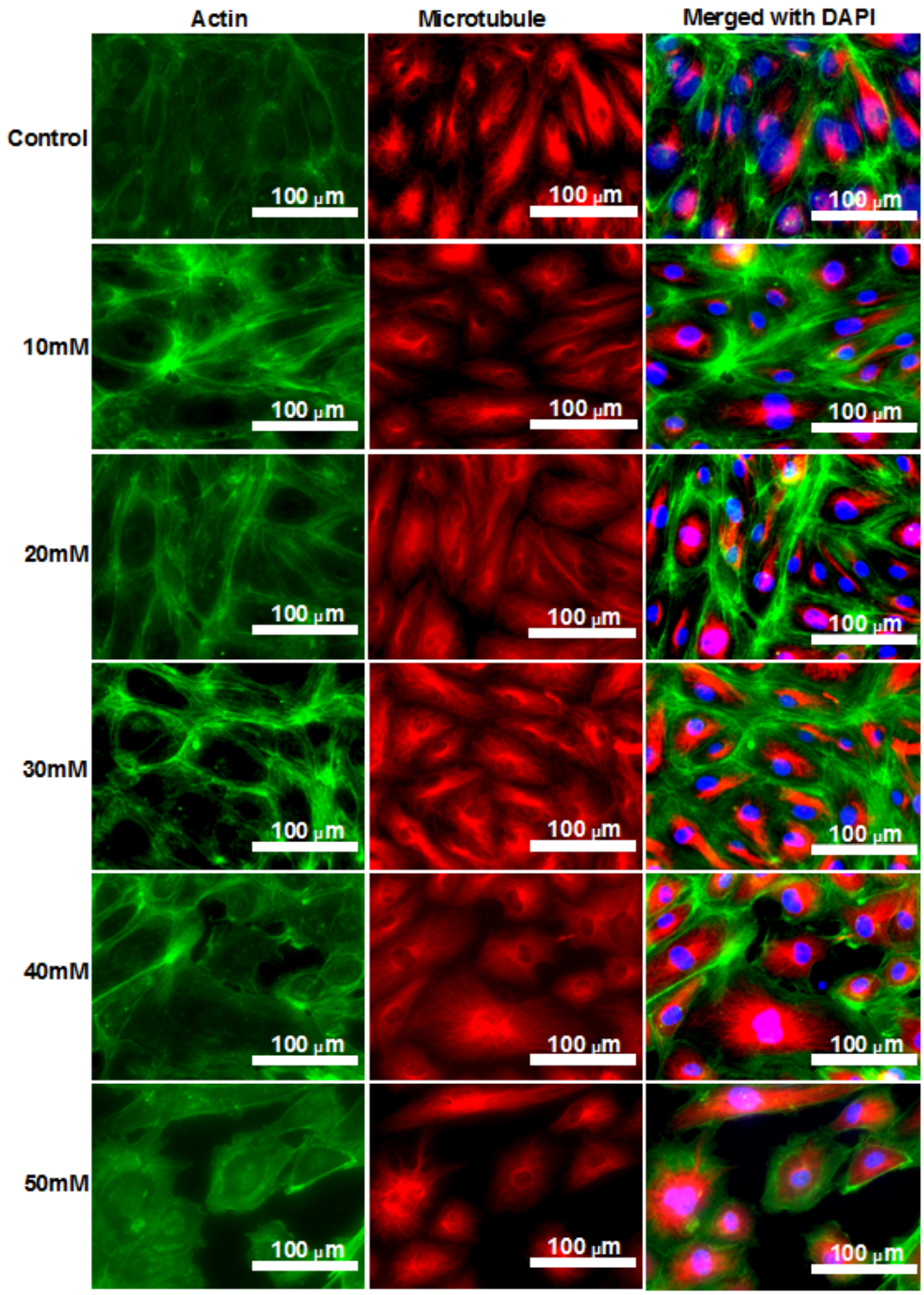

Figure 6. Cytoskeleton staining images of ECs treated by ECM supplemented with $MgCl_2$.

Cell morphology and microtubule structure were not significantly affected as the increase of $MgCl_2$ concentration. Some small green fluorescent dots were visible in all groups. Ventral

stress fibers which are actomyosin bundles connected to focal adhesions at both ends [97], were observed in all groups. At 10 mM and 20 mM $MgCl_2$, increased amount of thicker ventral stress fibers and nebulous fluorescence were displayed. Stress fibers were arranged along the edges of each cell and microtubule network was surrounded by the actin stress fibers in the 30 mM group. There were some discontinuities within the intercellular cell-to-cell junctions as the $MgCl_2$ concentration increased to 40 mM. The discontinuous areas got larger when $MgCl_2$ increased to 50 mM. A few ventral stress fibers were visible and cells were fraught with nebulous green fluorescence at 50 mM group.

Normalized actin fluorescent intensity per cell (*Figure 7*) showed that total cellular actin significantly increased when supplement $MgCl_2$ concentration was within 10 to 40 mM whereas actin quantity was not significantly different from that of control group when $MgCl_2$ increased to 50 mM ($n=12$, $P<0.05$).

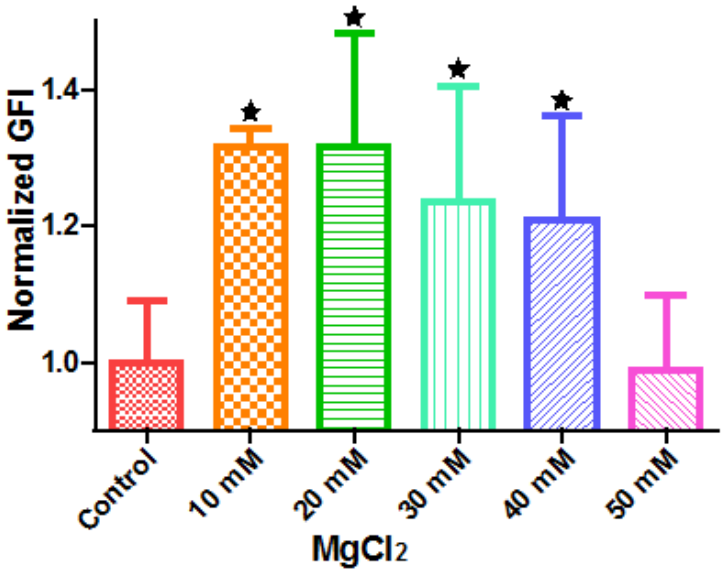

Figure 7. Normalized green fluorescence intensity (GFI) of ECs actin microfilament. Stars indicate GFI significantly different from control.

4.1.6 EC gene expression. We used a gene array for endothelial cells to examine the gene expression profile under the influence of Mg ion. Gene functions are classified into 7 different groups (Vaso C&D represents vasoconstriction & vasodilation). X-axis represents different gene functions and Y-axis represents the number of genes significantly changed. The bars above the X-axis are the up-regulated genes and below are the down-regulated genes. (n=3, P<0.05) We used a gene array for endothelial cells to examine the gene expression profile under the influence of Mg ion.

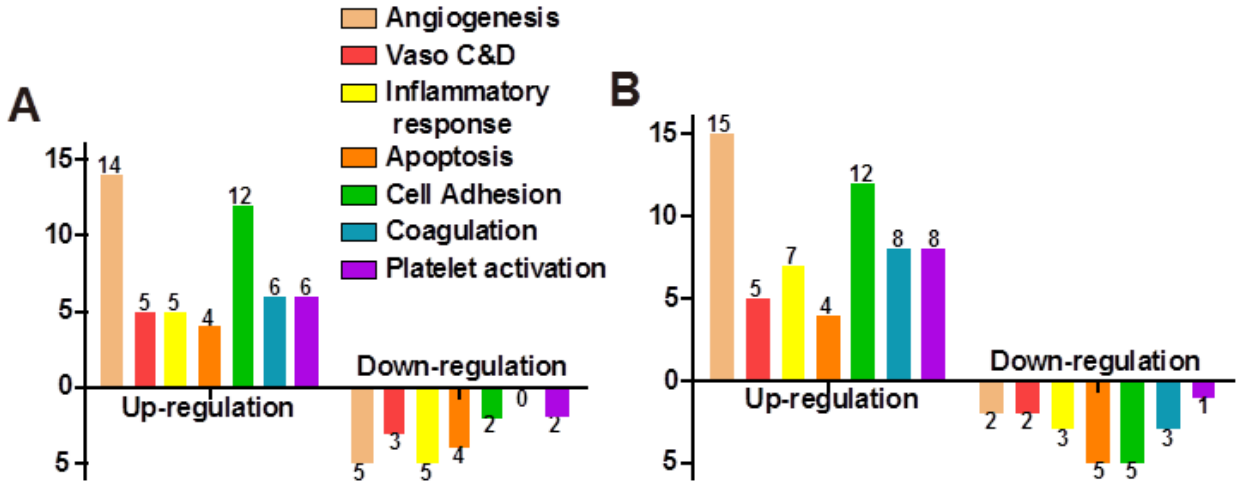

Figure 8. ECs gene expression after treated by ECM supplemented with 10 mM $MgCl_2$ (A) and 50 mM $MgCl_2$ (B).

In the 10 mM $MgCl_2$ group, 12 genes were excluded due to the absence of distinctive melting peak. Among the total of 72 detectable genes, 26 were up-regulated and 7 were down-regulated (*Figure 8*A). The remaining 39 did not show significant change. Table 9 summarizes some significantly changed genes under 10 mM of $MgCl_2$ (n=3, P<0.01). The expression fold change of FGF1, FLT1, FN1, MMP1, NOS3, and PROCR was more than 2 times that of the control. The majority of genes affected were related to angiogenesis and cell adhesion signaling pathways. As for the 50 mM $MgCl_2$ group (*Figure 8*E), 31 genes were up-regulated and 9 genes

were down-regulated. 15 of the up-regulated genes are involved in the angiogenesis signaling pathway and 12 up-regulated genes are related to cell adhesion signaling pathway.

Table 9

Gene expression changes of HCAECs (ECM supplemented with 10 mM $MgCl_2$ with normal ECM as control)

Gene	Function	Average fold change*
ACE	Angiogenesis	1.978
FGF1	Angiogenesis, Cell adhesion	2.415
FLT1	Angiogenesis	2.124
FN1	Angiogenesis, Inflammatory response, Cell adhesion, Coagulation, Platelet activation	2.383
HMOX1	Angiogenesis, Vaso-C&D, Inflammatory response, Apoptosis	1.799
IL6	Angiogenesis, Vaso-C&D, Inflammatory response, Apoptosis	0.624
IL7	Apoptosis,	0.518
ITGAV	Cell adhesion	1.762
MMP1	Coagulation	2.087
NOS3	Angiogenesis, Vaso-C&D, Platelet Activation	3.429
PGF	Angiogenesis	1.337
PROCR	Coagulation	2.264
TIMP1	Coagulation, Platelet activation	1.779
VEGFA	Angiogenesis, Cell adhesion, Platelet activation	1.360

*(Percentage of control, $P<0.01$)

In Table 10, AGTR1, ANXA5, CCL2, CCL5, FGF1, FN1, ITGAV, PLAT, and VCAM1 were up-regulated more than 2-fold higher than that of the control. IL7, PF4, PTGIS, SELE, and SELL were down-regulated to less than 0.5-fold of control. Among them, FLT1, NOS3, MMP1 and PROCR were the most significantly affected genes (fold change > 2, $P<0.01$) at 10 mM $MgCl_2$ but interestingly, they did not show significant changes at 50 mM. FGF1 and FN1 were up-regulated at both concentrations.

Table 10

Gene expression changes of HCAECs (ECM supplemented with 50 mM $MgCl_2$ with normal ECM as control)

Gene	Function	Average fold change*
AGTR1	Angiogenesis	3.014
ANXA5	Apoptosis, Coagulation	2.356
CCL2	Angiogenesis	4.290
CCL5	Angiogenesis, Inflammatory response, Apoptosis	8.413
FGF1	Angiogenesis, Cell adhesion	3.486
FN1	Angiogenesis, Cell adhesion, Inflammatory response, Coagulation, Platelet activation	2.300
IL7	Apoptosis	0.403
ITGAV	Cell adhesion	2.736
PF4	Apoptosis, Coagulation, Platelet activation	0.453
PLAT	Coagulation	5.140
PTGIS	Vaso-C&D	0.424
SELE	Inflammatory response, Cell adhesion	0.277
SELL	Cell adhesion, Coagulation	0.393
TIMP1	Coagulation, Platelet activation	1.439
VCAM1	Inflammatory response, Cell adhesion	3.436

*(Percentage of control, $P<0.01$)

4.2 Biocompatibility of Mg-RE Alloys.

4.2.1 Electrochemical corrosion properties. Potentiodynamic polarization curves of four RE alloys and pure Mg in HBS are shown in *Figure 9*A. An obvious shift of E_{corr} in cathodic direction and reduction in cathodic current density were observed in R3 and R4. The current density in all alloys decreased significantly compared with pure Mg. The E_{corr}, I_{corr} and corrosion rate of all Mg materials were summarized in *Figure 9*B. The corrosion rates of three RE alloys were 3 to 10 times lower than that of pure Mg.

A

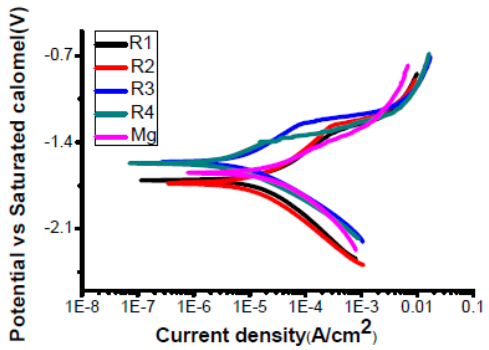

B

Material	E_{corr} (V)	I_{corr} (uA)	Corrosion rate(mm/y)
Mg	-1.580	46.80	0.153
R1	-1.710	17.50	0.057
R2	-1.730	11.60	0.038
R3	-1.560	6.440	0.017
R4	-1.540	3.760	0.027

Figure 9. Potentiodynamic polarization curves of Pure Mg and Mg-RE alloys in HBS (A). Electrochemical corrosion data of Pure Mg and Mg alloys (B).

4.2.2 Hemolysis rate. The hemolysis rates (HR) of the materials are shown in *Figure 10*. All the hemolysis rates of the materials were smaller than 0.6 %, much lower than the 5 % threshold, therefore, all samples were considered non-hemolytic according to the ISO 10993-4:2002 standard [98,99]. There was no significant difference among all the Mg materials tested.

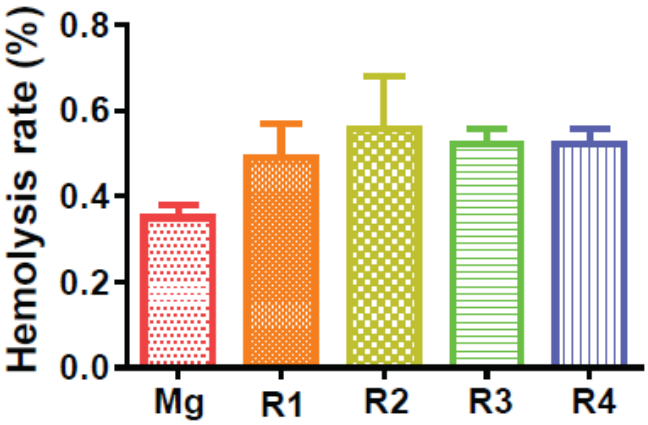

Figure 10. Hemolysis rate of diluted whole human blood incubated with Mg materials for 1 h.

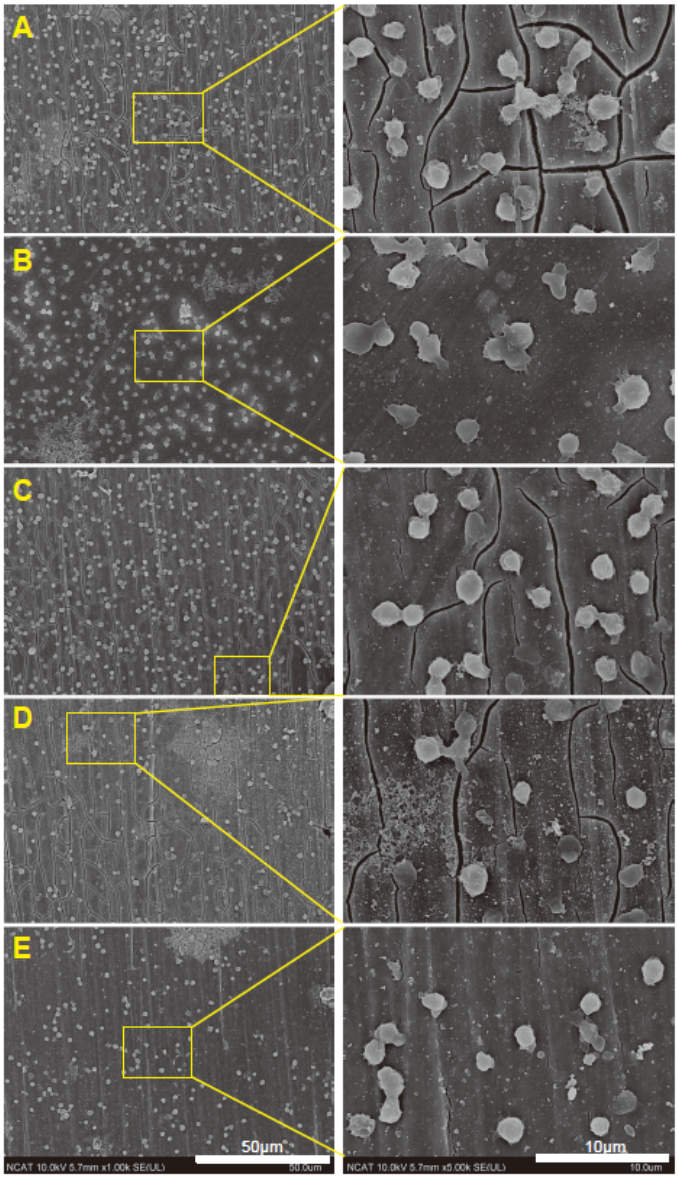

Figure 11. Representative SEM images of platelet adhesion and activation on Mg materials: (A) pure Mg, and (B-E) R1-R4.

4.2.3 Platelet adhesion. *Figure 11* shows the platelet adhesion and activation after incubation on the material surfaces for 1 hour. Activated platelets with spreading dendriticals connecting with their proximal platelets were observed on the pure Mg surface. In addition, a few platelets with long dentritical structure were seen under higher magnification. R1 and R2

had similar density of adherent platelets but with less spreading dendriticals compared to pure Mg. On the other hand, the number of adherent platelets on R3 and R4 was significant less than that on pure Mg (*Figure 12*).

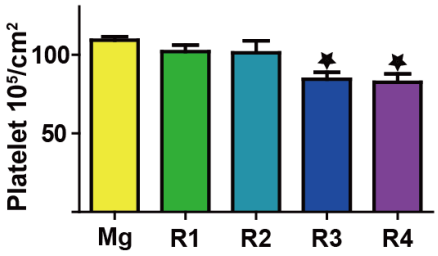

Figure 12. The number of adherent platelets. Star indicates that the platelet number is significantly different from that of pure Mg group ($P < 0.05$).

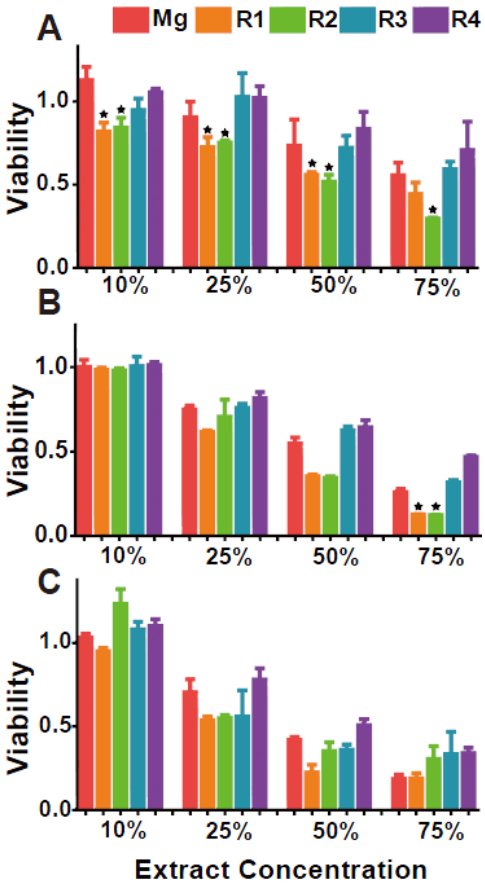

Figure 13. HAECs viability by MTT after treated with different Mg material extracts for 2 days (A), 4 days (B), and 7 days (C).

4.2.4 Indirect EC viability. MTT cell viability on days 2, 4 and 7 with different concentrations of alloy extract solutions is shown in *Figure 13*. Stars indicate that the cell viability is significantly different from that of pure Mg group ($P<0.05$).The overall cell viability for all groups decreased as the concentrations of the extract solutions increased. Extract solution of R3 and R4 didn't affect cell viability at any concentrations compared with pure Mg. On the 2nd day, reduced cell viability was observed in R1 and R2. On day 4, there was no significant difference among all the materials and pure Mg control except for R1 and R2 at 75 % concentration. On day 7, cell viability of all alloys was not significantly different from pure Mg control. Representative optical images of HAECs on day 7 were shown in *Figure 14*. Red arrows indicate the cell debris and dead cells. Cells all looked healthy, and there were no obvious morphological changes for all groups at 10 % and 25 % extract solutions. There were some dead cells and debris floated around when the extract concentration reached 50 %. In 75 % group, the cell density decreased significantly, especially for the pure Mg.

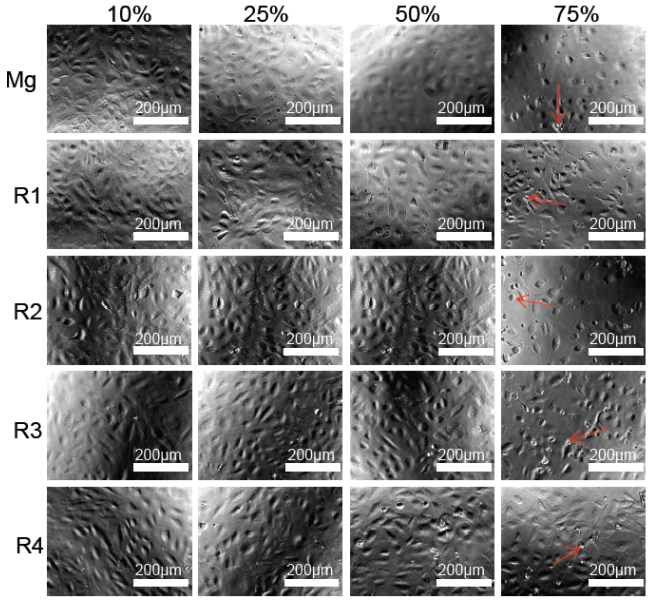

Figure 14. Representative optical images of HAECs morphology after treated with Mg material extracts for 7 days.

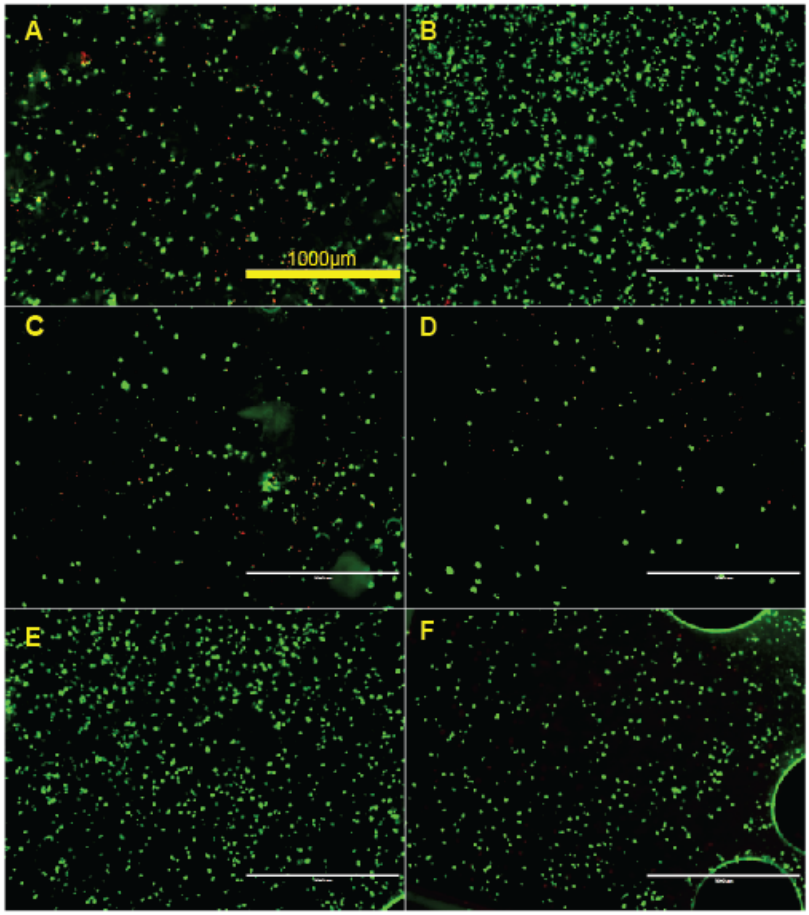

Figure 15. Representative fluorescent images of ECs on Mg materials after 3 h: (A) Pure Mg, (B) Tissue culture plate, and (C-F) R1-R4.

4.2.5 Direct Endothelialization. The attached HAECs were detected by fluorescent staining with green for live cells and red for the dead. The density of attached cells after 3 hours on R1 and R2 were lower than that on pure Mg, tissue culture plate, R3 and R4 (*Figure 15*). Most of the cells attached on the sample surface in all tested materials were still in round shape. Some dead cells could be observed on pure Mg, R1, and R2. In comparison, a few completely spread cells in healthy shape were seen on tissue culture plate, R3 and R4.

After 24 hours, most cells on pure Mg were dead, and many air bubbles with diameter of ~50 µm evolved on the surface of all the materials (*Figure 16*). More cells survived on R1 and

R2 compared to pure Mg but were in a stressed condition. On R3 and R4, majority of the attached cells were still viable, and they looked healthy and well attached, spreading in a spindle shape. However, cell density on R3 and R4 significantly decreased compared to that on the tissue culture plate control.

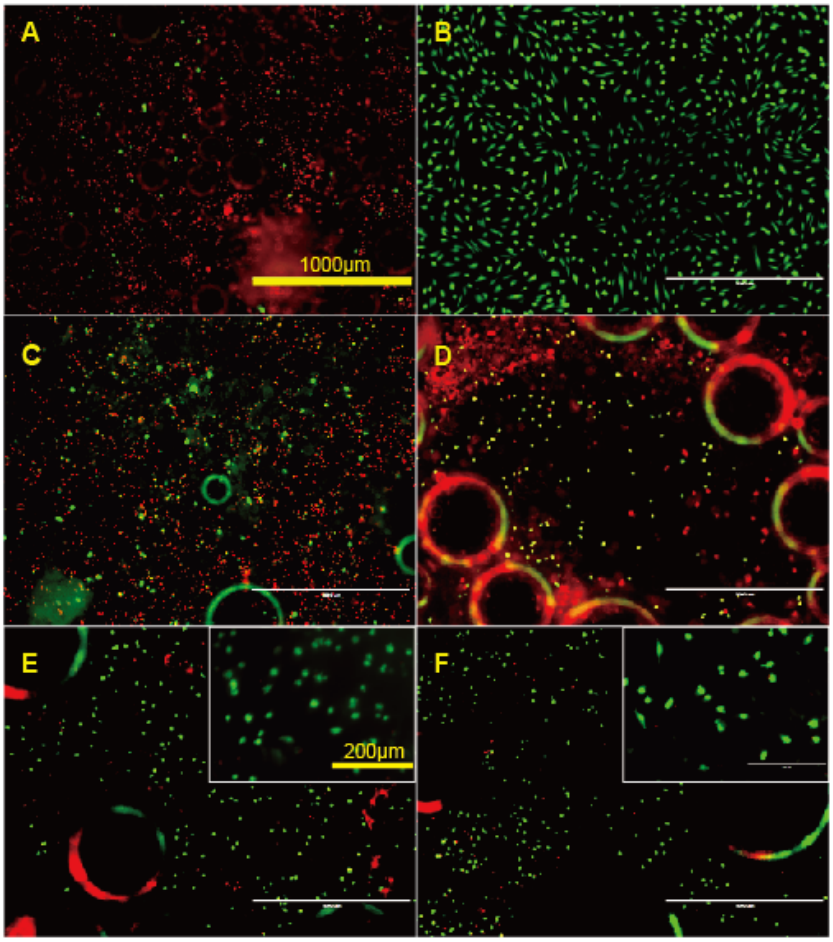

Figure 16. Representative fluorescent images of ECs on Mg materials after 24 h: (A) Pure Mg, (B) Tissue culture plate, and (C-F) R1-R4.

4.3 Collagen Self-assembly on Mg and Subsequent Cell Attachment.

4.3.1 Effect of collagen concentration. Collagen self-assembly with different concentrations of collagen monomers on SS Mg and SS AZ31 at neutral *p*H was examined first (*Figure 17*).

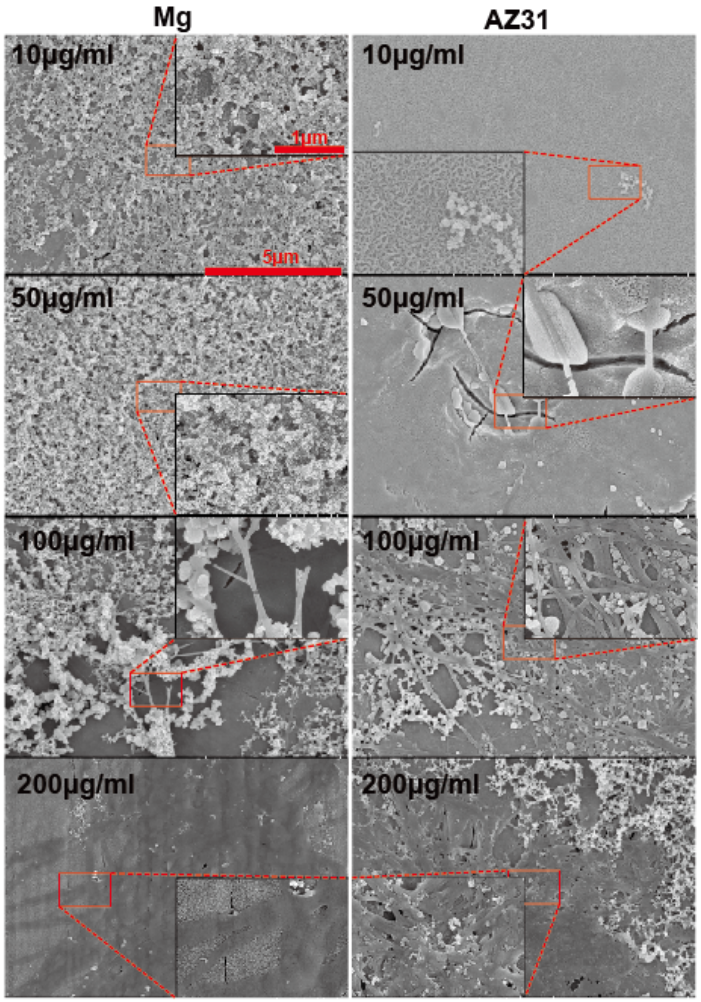

Figure 17. Representative SEM images of collagen self-assembly on Mg and AZ31.

The concentration of collagen monomer is marked on the upper left corner of each images. On pure Mg, collagen monomers agglomerated into a non-uniform structure and no long fibril was observed when the concentration was lower than 50 μg/ml. Some spherical particles were present on the surface of pure Mg in both 10 μg/ml and 50 μg/ml groups. When the collagen concentration reached to 100 μg/ml, a few fibrils started to appear. The structure changed from thin fibrils to wide bands as the initial concentration increased to 200 μg/ml. On AZ31 surface, long fibril started to appear as the collagen concentration reached to 50 μg/ml. In addition, sparsely dispersed woven structure composed of collagen fibers (fibril bundles) were

observed in the 100 µg/ml group. Multiple-layer network structure with collagen ribbon of 100 nm width was the predominant structure in the 200 µg/ml group. Spherical particles in different sizes were present in all the groups.

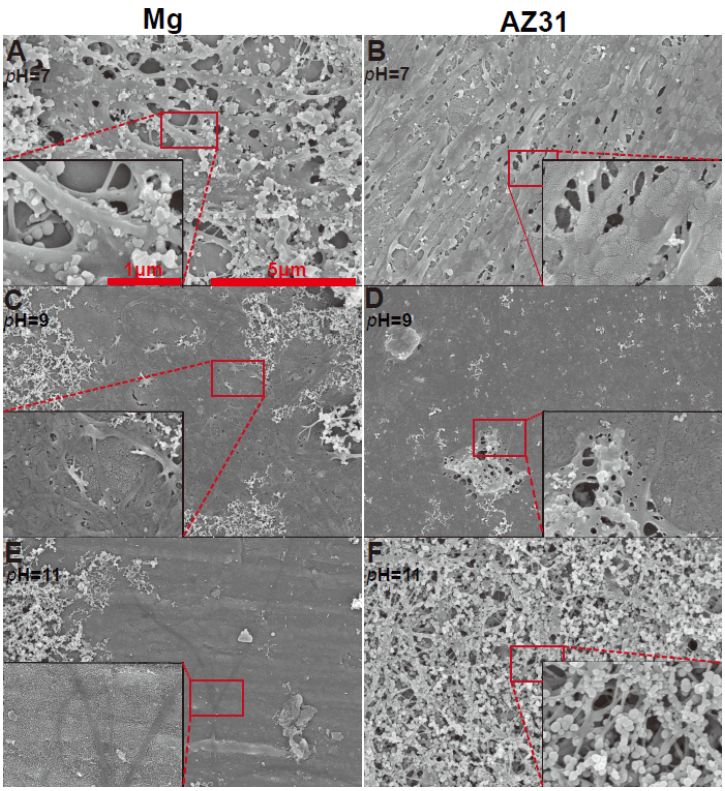

Figure 18. Representative SEM images of 200 µg/ml collagen self-assembly in DPBS with different *p*H values.

4.3.2 Effect of *p*H. Effect of *p*H on collagen assembly was also investigated. SEM images of collagen self-assembly under different *p*H on SS materials for 2 hours are shown in *Figure 18*. At *p*H 7, collagen ribbons with width ~100 nm conjugated with other fibrils, forming a multiple layer network structure on pure Mg. A few nanofibril side chains connecting adjacent long collagen ribbon were also seen. On AZ31, some parallel collagen ribbons were connected with adjacent collagen ribbons by smaller branches and others merged with their proximal collagen, forming a uniform sheet. At *p*H 9, more collagen ribbons wove together spreading on

Mg surface. In addition, some bare areas and crevices were observable. The whole surface of AZ31 was almost covered by a collagen layer with some small holes. Few long collagen fibrils were present on pure Mg when *p*H rose to 11. On AZ31, thin fibrils randomly crossed with others, resulting in a network structure. A lot of nano-spherical particles attached to the collagen fibrils.

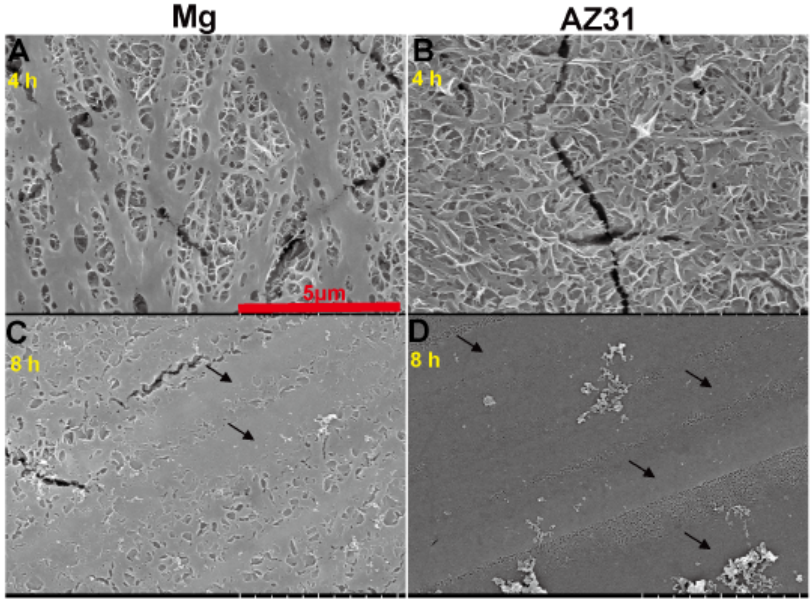

Figure 19. Representative SEM images of 200 μg/ml collagen self-assembly on Mg and AZ31 for 4 h and 8 h.

4.3.3 Effect of reaction time. *Figure 19* shows the structures of collagen assembling for different time periods on SS materials at neutral *p*H. The concentration of collagen solution is 200 mg/ml. Arrows in black color indicates the large fiber bands. After 4 hours assembling, a cancellous underneath layer was covered by some long collagen ribbons on pure Mg. Similar cancellous structure was found on AZ31, but less thin collagen fibrils could be observed on the top. When the assembly time reached 8 hours, micrometer-wide fibers were present on both pure Mg and AZ31. On pure Mg, a lot of small lamellar sheets were observed between two thick fibers.

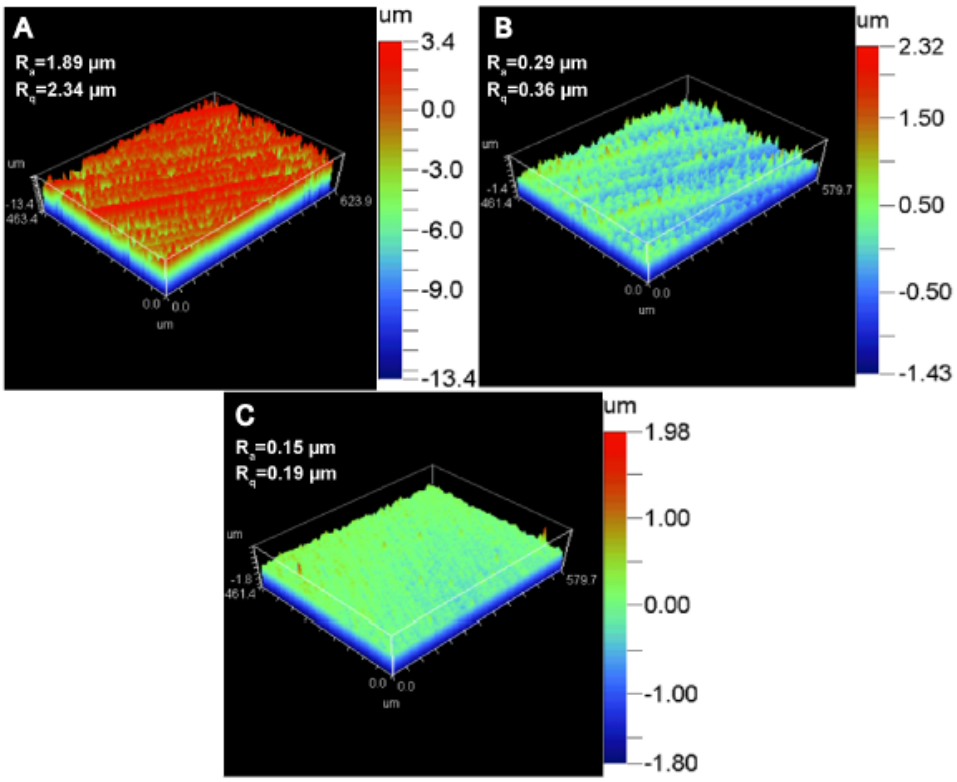

Figure 20. 3-D surface topography of Mg sample polished by different SiC paper (A: 180 grit; B: 800 grit; C: 1200 grit).

4.3.4 Effect of surface roughness. Representative 3-D topographical images of materials after polished by different SiC paper are shown in *Figure 20*. The average roughness (R_a) and the corresponding root mean squared roughness (R_q) were also calculated (*Figure 20*). *Figure 21* shows the collagen self-assembly on the samples with different surface roughness. On the RS Mg materials, long collagen fibers interwove with each other resulting in a compact woven layer with a few fish-like scales on the top. The woven layer on RS AZ31 was less dense compared with that on RS Mg. Larger and more fish-like scales structures could be seen on the RS AZ31. For both AZ31 and pure Mg with SR, collagen fibers aligned parallelly to each other at some places while randomly intertwined at other places. On SS of both materials, collagen bands were similar as described previously (*Figure 17*).

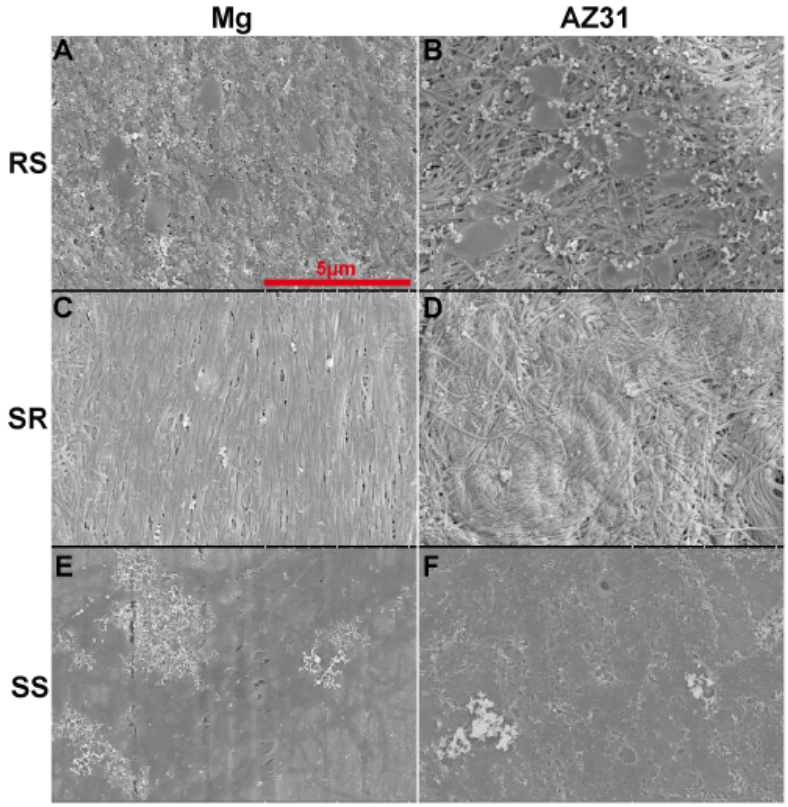

Figure 21. Representative SEM images of 200 mg/ml collagen self-assembly on Mg (A, C, E) and AZ31 (B, D, F) with different surface roughness (A–B: RS; C–D: SR; E–F: SS).

4.3.5 Collagen assembly quantification. We also quantified the amount of collagen on the material surface during its assembly. A standard curve for quantification of collagen content was established (*Figure 22*A). The optical absorbance at 540 nm versus collagen content displayed reasonable linearity within the range from 5 to 60 μg/ml. Collagen dynamic adsorption curves on Mg and AZ31 surfaces are shown in *Figure 22*B and *Figure 22*C. For both AZ31 and pure Mg, less collagen was able to be absorbed onto the SS materials at the initial phase (0.5 h) compared with RS and SR materials. The amount of attached collagen increased as the adsorption time increased and reached equilibrium state after 4 h for all three groups of AZ31. Collagen on the pure Mg with SS kept increasing slowly from 0.5 to 2 h. In comparison, collagen on pure Mg with RS peaked at 2 h and then started to drop. Among all the groups, the highest

amount of adsorbed collagen was 30.69±1.96 µg on RS Mg at 2 h. Two-way ANOVA analysis revealed that both time and surface roughness had significant effect on collagen adsorption on pure Mg.

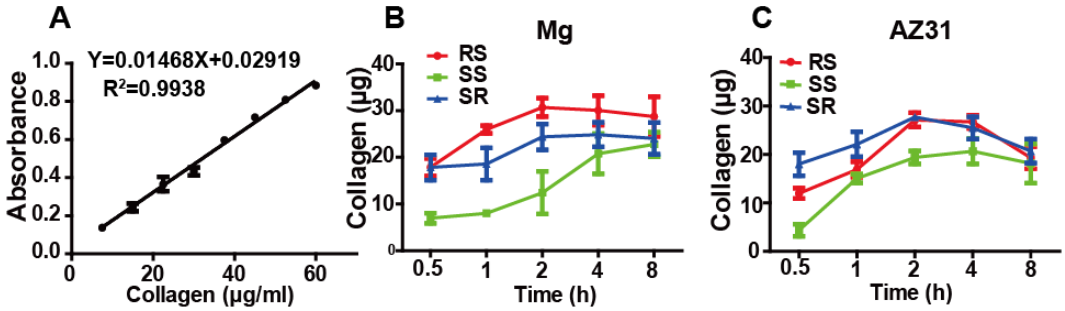

Figure 22. Collagen adsorption quantification. Standard curve for quantification of collagen (A). The amount of collagen absorbed on Mg (B) and AZ31 (C) with different surface roughness.

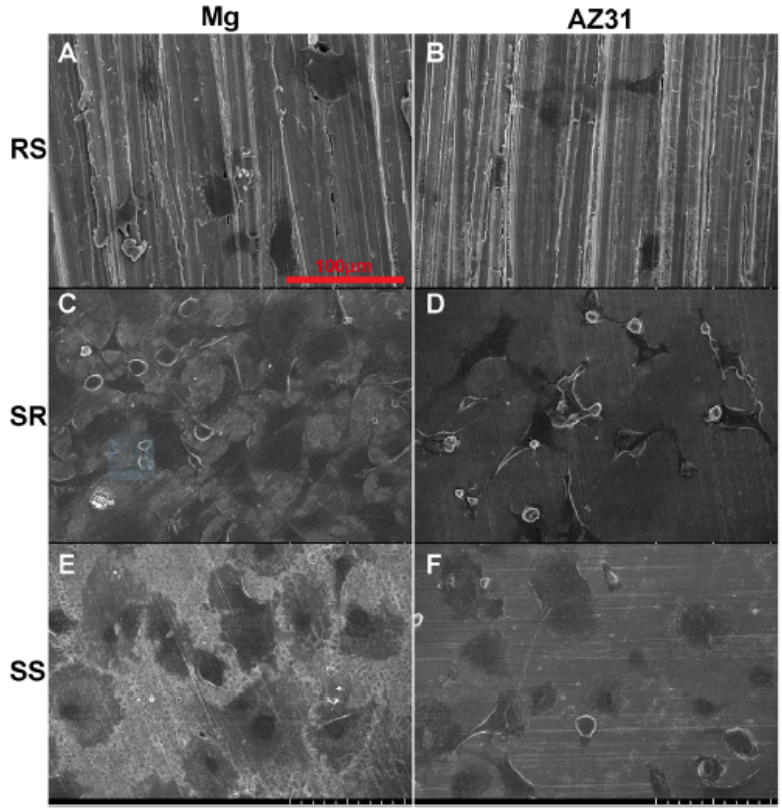

Figure 23. Representative SEM images of MC 3T3 cell attachment on collagen self-assembled at Mg and AZ31 with different surface roughness.

4.3.6 Bone cell attachment and proliferation. After Mg and AZ31 with different surface roughness were treated by 200 µg/ml collagen solution for 2 h, the materials were used to test subsequent bone cell attachment (*Figure 23*). SEM images showed that both round cells and cells with filopodia were observed on RS AZ31 and pure RS Mg. On SR materials, most cells were well attached with flattened morphology and a few fibroblast-like cells with webbing could also be seen. In addition, super long filopodia from some cells span over a large distance and reached the edge of other cells or an empty area. On the SS materials, most cells were well flattened with very large cell surface area. Cell density on SR and SS was significantly higher than that on RS.

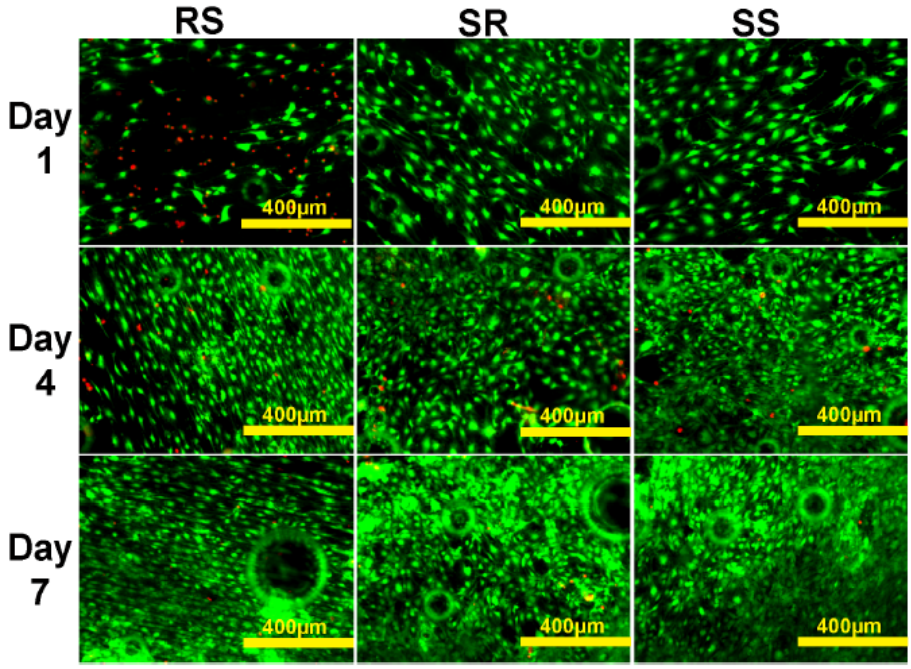

Figure 24. Representative fluorescent images of MC 3T3 cells growing on collagen self-assembled at AZ31 with different surface roughness for 1, 4 and 7 d.

Fluorescent live/dead cell analysis was then performed to examine the bone cell proliferation. MC 3T3 cells on AZ31 and Mg treated with 200 µg/ml collagen solution for 2 h are shown in *Figure 24* and *Figure 25*, respectively.

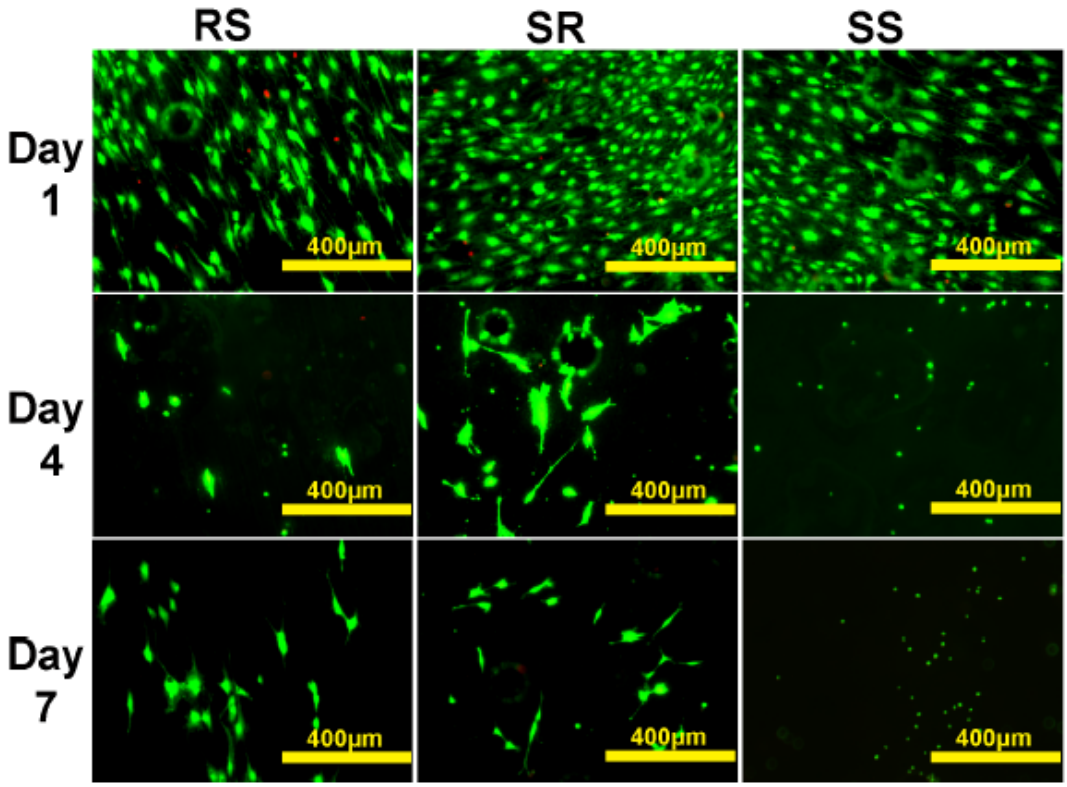

Figure 25. Representative fluorescent image of MC 3T3 cells growing on collagen self-assembled at Mg with different surface roughness for 1, 4 and 7 d.

Cells displayed healthy morphology in all the groups after one day. Cell densities on SR and SS AZ31 were significantly higher than that on RS AZ31 (*Figure 24*). Some dead cells were visible after first day on RS AZ31. Small gas bubbles were present in all the materials. After three days' incubation, cell density on all the AZ31 materials increased. On the RS AZ31, cells elongated at the same direction. After seven days, cell density further increased and multiple layers of cells could be seen in all the three groups. Most of the cells on the RS group still aligned in the same direction. Larger gas bubbles emerged in all groups. On pure Mg, cell densities significantly decreased at 4^{th} and 7^{th} day. At the first day, cells showed similar uniform elongation on the RS pure Mg. However, normal spreading cells could barely be observed on the SS Mg at 4^{th} and 7^{th} day.

Table 11

pH value of the cell culture media after incubated with cells on materials

Material		*p*H		
		1 day	4 day	7 day
AZ31	RS	7.93±0.05	7.88±0.03	7.94±0.03
	SR	7.70±0.08	7.92±0.03	7.85±0.05
	SS	7.75±0.08	7.91±0.06	7.76±0.07
Mg	RS	8.30±0.14	7.95±0.03	7.96±0.03
	SR	8.01±0.06	7.92±0.03	7.92±0.03
	SS	8.13±0.06	7.95±0.03	7.87±0.03

Table 11 summarizes the *p*H value of cell culture media during the culture. In both AZ31 and Mg groups, the materials with RS showed significantly higher *p*H change than the materials with SR and SS after the first day. Mg^{2+} concentration (*Figure 26*) after collagen was incubated with Mg and AZ31 of different surface roughness for 2 h was all around 25 mM (Error bars were omitted for clarity purpose). In contrast, Mg^{2+} concentration in the cell culture media was significantly lower than that in the collagen solution for the AZ31 group from 1 day to 7 day.

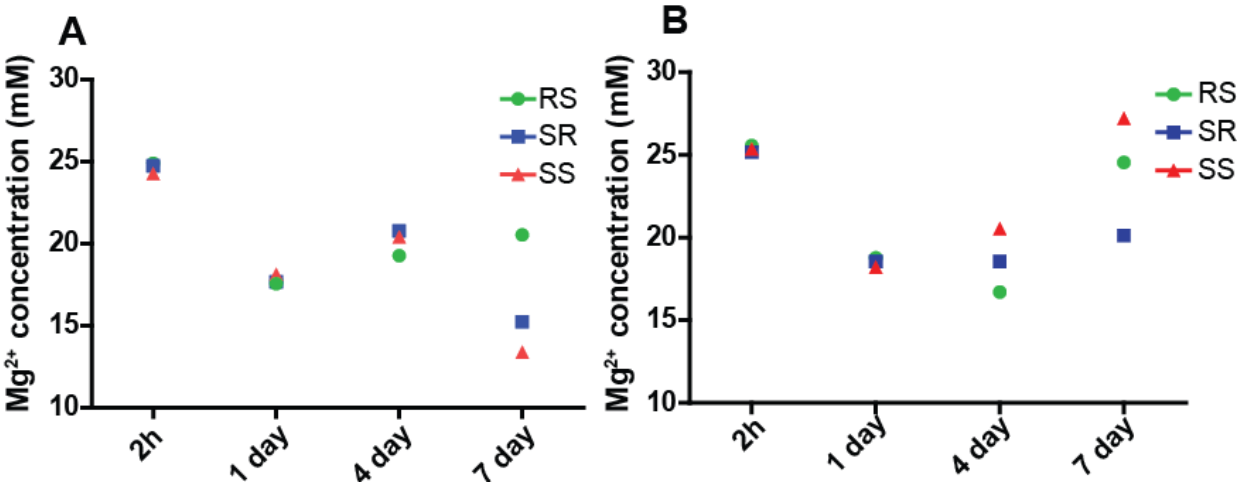

Figure 26. Mg^{2+} concentration after the materials (A-AZ31; B-Mg) were incubated with collagen solution for 2 h and cocultured with cells for 1, 4 and 7 days.

4.4 Endothelialization of Mg-RE Alloys with Fluoride and Collagen Coating.

4.4.1 Surface morphology of HF conversion coating. Surface morphology of the three materials after treated with HF for 3 days was shown in *Figure 27*. Pure Mg surface was converted into a layer of granular and columnar structure. The diameter of the granules was ~50 nm and the length of the columnar structure was ~200 nm. In both R1 and R2, the granular structures from the converted layers were much smaller than that on the pure Mg surface. Compared to pure Mg, grain size refinement by rare earth elements or direct reactions between rare earth elements with HF may cause such finer porous structures on HF treated Mg-RE alloys. The addition of Zn in R2 could be the reason for the different alignment of the granular structure.

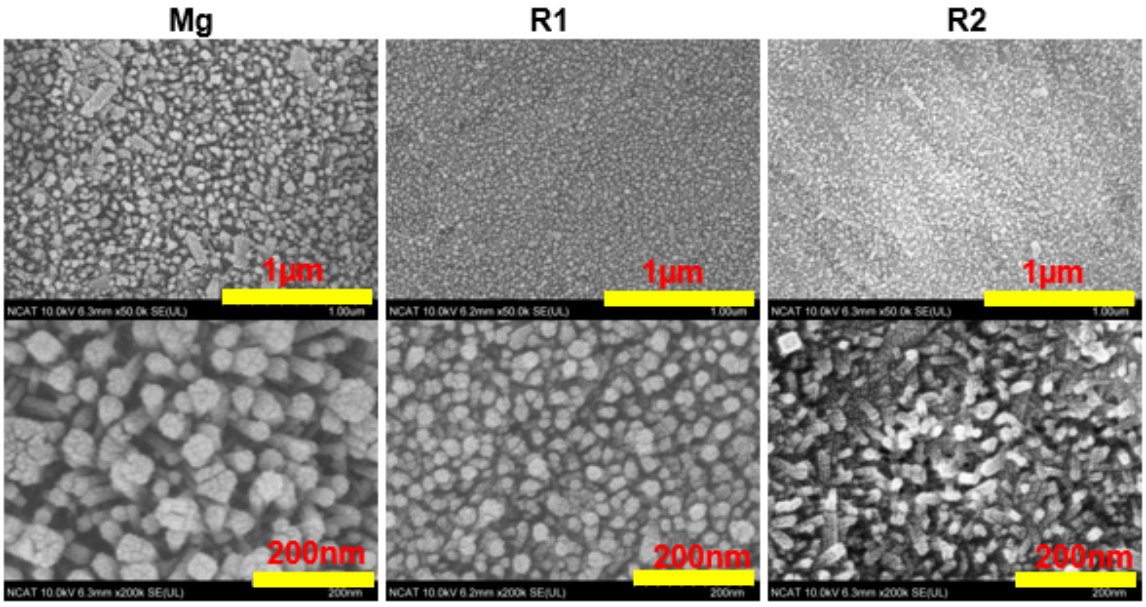

Figure 27. SEM images of fluoride coating morphologies.

The coating thickness in all samples was about 20 µm (*Figure 28*). The first row is the SEM images displaying cross sections of Mg fluoride coating in epoxide resin. The images at the second row and third row are EDS mapping (Mg in green color, fluorine in red color). Transection images of SEM showed that there was a distinctive boundary between Mg substrate and the MgF_2 modified layer.

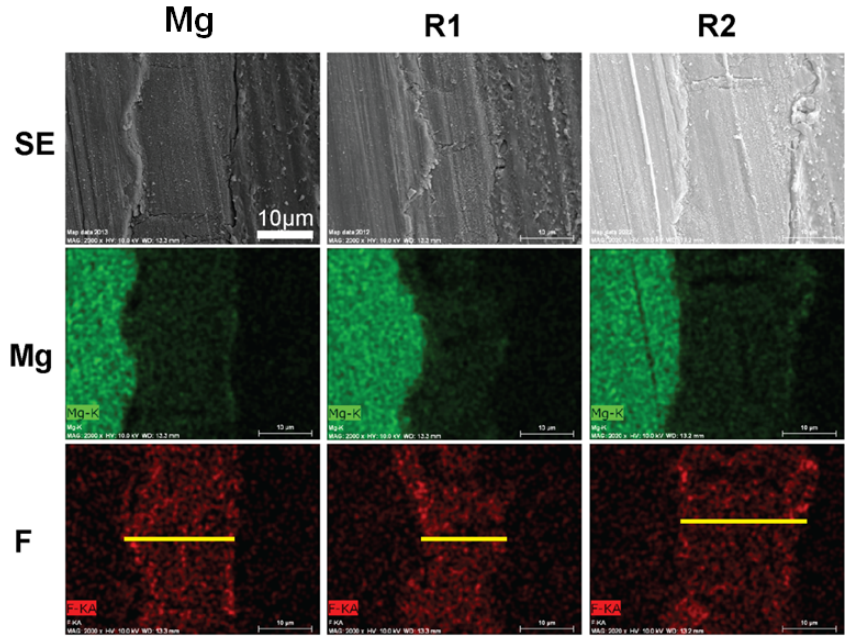

Figure 28. EDS Mapping for cross section of fluoride coating. (Scale bar: 10.0 μm).

4.4.2 Endothelialization on coated Mg material. Live/Dead kit including calcein AM and Ethidium homodimer-1 (EthD-1) was used to test how cells directly interact with alloys and coatings. Calcein AM could be metabolized by ubiquitous intracellular esterase activities resulting in presence of green fluorescence in live cells. EthD-1 is excluded by the intact plasma membrane of live cells. Upon binding to nucleic acids, the emission intensity of EthD-1 at 635 nm undergoes a 40-time enhancement. Representative images of direct endothelialization for 1, 2, and 3 days on bare Mg, Mg coated with collagen and Mg treated with HF are shown in

Figure 29. HF treated Mg yielded most attached and viable cells (green) in all groups. Cell density slightly decreased from 1st day to 3rd day on pure Mg treated with HF. For the non-treated pure Mg control group, some dead cells (red) were still observed on the very first day but none were observed either on day 2 or 3. A few live cells appeared on the surface of collagen coated Mg but the density was much lower than that on Mg treated with HF. In addition, on days 2 and 3 only, dead cells could be seen on collagen coated group. Collagen coating was used as

positive control in this study since it is the most abundant extracellular matrix protein which provides adhesion points for cell attachment and migration.

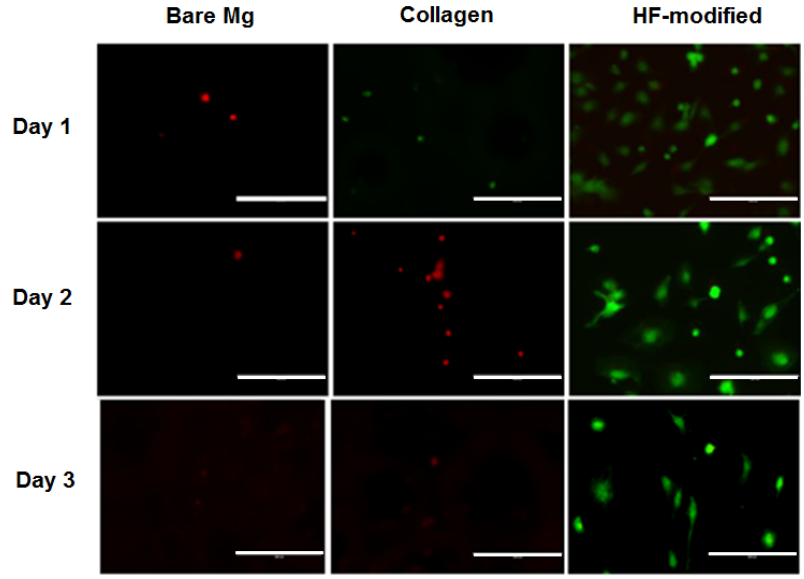

Figure 29. Endothelial cells cultured on bare Mg, collagen coated Mg and HF treated Mg from day 1 to day 3. (Scale bar: 10.0 µm).

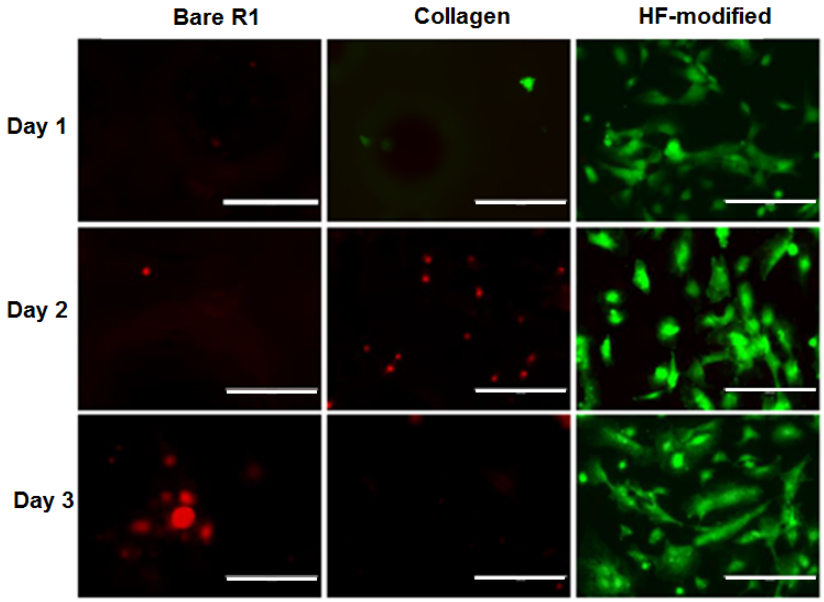

Figure 30. Endothelial cells cultured on bare R1, collagen coated R1 and HF treated R1 alloys from day 1 to day 3. (Scale bar: 10.0 µm).

Figure 30 shows the representative images of direct endothelialization on bare R1, R1 coated with collagen and R1 treated with HF. Results were similar to that of pure Mg group. Fluoride treated R1 had most viable cells while bare R1 had the least. Better cell attachment was shown in HF treated R1 group on the 1st day compared to the same one in pure Mg group. Also, cell density on the 3rd day in HF treated R1 group didn't decrease.

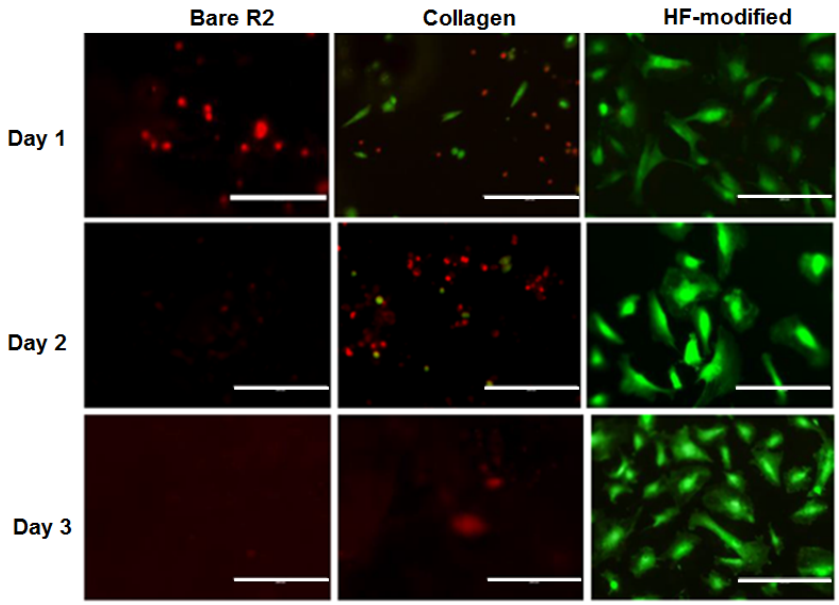

Figure 31. Endothelial cells cultured on bare R2, collagen coated R2 and HF treated R2 alloys from day 1 to day 3. (Scale bar: 10.0 μm).

Cell attachment and proliferation on R2 group (*Figure 31*) were very similar to that in the R1 group. The most different one was the collagen coated group, and much better endothelialization was observed compared with R1 and pure Mg groups. Some fully spreading cells appeared at the very first day which demonstrated that collagen could improve the cytocompatibility to a certain degree. On the second day, most cells were dead and only a few cells were alive however in a stressed condition.

CHAPTER 5

Discussion and Future Research

5.1 Discussion

5.1.1 Endothelial responses exposed to metal ions. Endothelial cells form a semi-permeable endothelium monolayer which separates the blood components from the underlying tissues. It plays important role in immune response, coagulation, growth regulation, modulation of blood flow and production of extracellular matrix [100]. After a stent is deposited into the blood vessel, the surface of the stent will directly contact endothelial layer. Re-endothelialization onto the inner layer of the stent is a very important step for vascular reprogram. Late restenosis, re-narrow of the blood vessels after stent implantation, is a major problem for current stent materials. The interaction between stent material and endothelial cells, therefore, is of great importance. Hence, we examined the responses of HCAECs after exposure to ions of different individual alloying elements.

The majority of the alloying elements will be released from the material during the course of degradation. However, it is hard to mimic the real *in situ* concentrations of different ions for the *in vivo* scenarios. The concentration of degradation production could be much higher at the local microenvironment of stent-endothelial interface than that in the blood stream or other tissues. Previous studies provide some information on the concentration of Mg ion after degradation of the alloys *in vitro*. For example, Mg^{2+} concentration in DMEM incubated with Mg-Ca alloy for 72 h was ~57.96 mM [101] and Mg^{2+} concentration in cell culture media after Mg-Nd-Zn-Zr alloy was co-cultured with human umbilical vein endothelial cells for 7 days was 9.53 mM [102]. Therefore, we used a concentration range of 10-100 mM for Mg ion in our *in vitro* tests. Technically, the final Mg^{2+} concentration is the summation of 3 mM $MgSO_4$ from the

ECM and additional supplemented $MgCl_2$. Since Mg is the major component of Mg-based alloy, the tested concentrations for other alloying elements Ca, Zn, Al and REs were much lower.

To rule out the potential interference from the Cl^- present in the solution, 10-200 mM NaCl solution was used and no significant effect on cell viability was observed up to 100 mM NaCl. Besides the direct effects of ions on cellular activities, *p*H and osmolality changes in the solution induced by the ions may also affect cells. We did not observe significant *p*H changes in all the final ion solutions used. As for osmolality, similar results were observed except when $MgCl_2$ concentration was higher than 66.7 mM. 66.7 mM $MgCl_2$ solution has the similar osmolality as 100 mM NaCl. Therefore, both osmolality stress and Mg^{2+} ion may play a role in reduced cell viability when $MgCl_2$ concentration is over 66.7 mM, the EC50 value in our case. Feyerabend et al. showed that the EC50 of $MgCl_2$ on MG63 cells and human umbilical cord perivascular cells (HUCPCs) were 53 mM and 73 mM, respectively [48]. The tolerance of HCAECs (EC50 of 66.7 mM) on $MgCl_2$ is between that of MG63 cells and HUCPCs. The EC50 of $ZnCl_2$ measured here for endothelial cells is ~130 μM, comparable to that of mouse macrophage cell line (~203.89 μM) [103]. The slight differences between these measurements are probably because of different types of cells. The *p*H and Ca^{2+} may also interfere with MTT assay. Our test showed that the absorbance of the blank control without cells significantly increased when the Ca^{2+} concentration is higher than 60 mM. This false positive result is most likely caused by the aggregates of sodium dodecyl sulfate in solution with excess Ca^{2+} [104]. It is also mentioned by Fisher et al. that highly alkaline environment may induce false-positive result as well [101]. Hence, MTT test should be applied with caution at the situations where *p*H is highly alkaline or the alloy degradation products include Ca^{2+}. The toxicity of REs on cells is most likely caused by the displacement of Ca^{2+} ion from functional biomolecules as they have

the similar radius as Ca^{2+} ion [105]. It was shown by Drynda et al. that REs under 100 μg/ml (around 500 μM) didn't lead to significant metabolic changes of smooth muscle cells [105]. Feyerabend et al. also demonstrated that REs under 1,000 μM didn't reduce human osteosarcoma cell line MG63 viability. All REE ions had significant toxic effects on endothelial cell viability when their concentrations were higher than 400 μM, indicating that endothelial cell is more sensitive to REs.

The effects of $MgCl_2$, $CaCl_2$, $ZnCl_2$, $AlCl_3$, and REs on HCAECs membrane were studied by LDH assay, which is also widely used to test the biocompatibility of Mg-based alloys [106-108]. LDH, an indispensable cytoplasmic enzyme for all cells, is rapidly released to extracellular space upon damage of the plasma membrane. Han et al. reported that the decreased LDH level in cells treated by 20 μg/ml $CuSO_4$ for 24 h is caused by LDH inactivation by Cu^{2+} [109]. Cells treated with $MgCl_2$, $CaCl_2$, $ZnCl_2$ and $AlCl_3$ all showed a decreased LDH tendency when the ion concentration is higher than certain thresholds. This may also be caused by the inactivation of LDH due to high ion concentration.

In comparison with LDH and MTT tests, BrdU is not dependent on direct enzymatic reaction so that the interference from Mg corrosion products is negligible. Based on this fact, some researchers believe that BrdU is a more appropriate test for cytotoxicity of Mg materials [110]. It was also shown that cell proliferation rate by BrdU assay was more sensitive than MTT test for some metal ions. For example, cell viability was not significantly affected at 30 mM $MgCl_2$ (*Figure 2*A) while the proliferation rate (*Figure 4*) was significantly reduced to 63±9%. Moreover, 20 mM $CaCl_2$ demonstrated significant inhibition on cell proliferation rate. This reduced proliferation is probably caused by ionic imbalance and production of reactive oxygen species (ROS). Ionic imbalance may lead to altered signaling pathway related to cell cycle,

reduced enzymes activities and increased DNA replication errors. It is well known that metal corrosion products can induce ROS production [111,112]. Extra $ZnCl_2$ can induce serious mitochondrial dysfunction and remarkable intracellular ROS production [112]. Depending on the level of ROS, it may increase the cell proliferation at low level or cause damages to DNA and other biomacromolecules, leading to decreased proliferation or even cell apoptosis at high level [113]. Therefore, higher cell proliferation rate at the low ion concentration was likely caused by lower amount of ROS induced by metal ions. As the metal ion concentration is increased, the increasing ROS production caused the dampened proliferation. Also, Mg^{2+} is a cofactor for DNA polymerase and other important enzymes participated in DNA replication. Previous study by Maier et al. showed that 10 mM $MgCl_2$ could stimulate endothelial proliferation [114], consistent with the BrdU proliferation result (114±0.70%) reported here.

Endothelial cell migration is essential for both angiogenesis and endothelialization. As the re-endothelialization on the stent progresses, the chance of coagulant molecules or platelets attaching to the stent reduces. We used scratch wound assay to study how Mg ion affect endothelial cell migration as it is a simple, inexpensive and very reliable method for cell migration study [115-117]. Our results show that at 10 mM and 20 mM, $MgCl_2$ increased the migration of endothelial cells within a few hours. This results is in line with a previous study by Banai et al. showing that 4 mM Mg^{2+} can stimulate capillary endothelial cell migration [118]. This might be a very beneficial characteristic for Mg-based stent materials if the degradation product concentration is maintained within this range. The exact mechanism responsible for this increased cell migration ability is not fully clear. One of the factors could be the fast assembling of actin cytoskeleton into stress fiber, filopodia, and lamillipodia [97]. Nitric oxide (NO) as an important cell migration, vasodilation and angiogenesis regulator may be another factor [119]. In

the 10 mM $MgCl_2$ treated group, NO synthase III (NOS3) was up-regulated to 3.429 fold of control. Up-regulated NOS3 may lead to enhanced production of NO and further increase cell migration ability. In addition, ROS generated by NADPH oxidase may also play an important role in endothelial cell migration by stimulating some redox signaling pathways [115].

However, higher $MgCl_2$ concentration of 50 mM not only decreased endothelial cell migration rate but also led to the detachment of a large amount of cells along the edge of the scratched wound. This could be due to the weakened cell-cell junctions and reduced cell-matrix adhesion. This interpretation is supported by the fluorescent staining result (*Figure 6*) where cell-cell connection was affected and some discontinuities between the cells could be observed when $MgCl_2$ was above 40 mM. The changes in junction protein expression could be one of the reasons. Vascular endothelial cadherin, platelet endothelial cell adhesion molecule (PECAM), occludin, claudin, and endothelial cell selective adhesion molecule (ESAM) are the major transmembrane adhesive proteins at endothelial junctions [120]. It was found that CDH5 (cadherin-5, type 2) was up-regulated to 1.56±0.16 fold of control at 10 mM $MgCl_2$ and 1.65±0.05 fold of control at 50 mM ($P<0.05$), respectively. Occludin and PECAM didn't show significant change. Further investigation is needed to explain the detailed changes of cell-to-cell junctions and cell-matrix adhesion.

Gene expression profile is another important way to study how cells interact with biomedical materials. It could suggest the subtle cellular regulation changes when metabolic changes of cells are not detectable. $MgCl_2$ at 10 mM and 50 mM had different effect on HCAEC gene expression in a concentration dependent manner. The expression fold change of CCL2 and CCL5 were 4.290 and 8.413 ($P<0.01$) respectively at 50 mM of $MgCl_2$ indicating strong inflammatory chemokines regulation [121]. Since Mg^{2+} is a ubiquitous cofactor for a lot of

biomacromolecules, it plays a wide range of roles in cell cycle and cell activities. Besides the direct effect of Mg^{2+} on enzymes, it is believed that increased Mg^{2+} could activate phosphorylation reactions of cell followed by changes of cellular signaling pathways [122]. The altered genes may have great potential to be used for gene-eluting stent. For instance, if down-regulation of a certain gene causes the suppression of one cellular activity, it could compensate for such a negative effect induced by the biomaterial by delivery of the down-regulated gene through eluting. One example is the endothelial NOS gene (eNOS), and it was used in gene-eluting stent [123]. Results showed that this eNOS-eluting stent demonstrated better re-endothelialization and significant reduction in neotintimal formation. Despite that identifying the effective target genes and successfully deliver to the local tissue could be challenging, this is a very promising strategy for new type of drug-eluting stents.

Nonetheless, the altered gene expression should not be interpreted as corresponding functional changes in the same way. More comprehensive studies on gene expression and protein expression are required to fully illustrate the underlying mechanisms. Mg-alloy degradation product often is a complex mixture of all the alloying elements. There is no doubt that the effect of individual elements on endothelial cells is important. The combinative effect of the mixture of those alloying elements should be further studied in the future as well in order to better understand how the degradation products affect endothelial cell activity as a whole.

5.1.2 Biocompatibility of Mg-RE alloys. Platelet morphological and biochemical changes are good indicators for hemocompatibility [124,125]. At the beginning of stent development, 20 % of self-expandable stents would suffer from subacute stent thrombosis [126]. Platelet activation and adhesion are the important initial steps of restenosis [127,128]. Individual platelets can be categorized as round, dendritic, spread-dendritic and fully spread corresponding

to different stages of activation. Static platelet adhesion test is the most convenient and accurate way to get information about whether the stent material will cause severe platelet adhesion in vivo. Because extracellular Mg ions can reduce the intracellular calcium ions, Mg alloys could inhibit platelet adhesion and aggregation [129]. We showed that the density of attached platelets on pure magnesium was the highest, and the morphology of the adherent platelets on all materials was almost the same, demonstrating that addition of RE elements into Mg alloys didn't trigger the platelet activation. It is still unclear how platelet activation was initiated. We speculate that the unspecific absorption of von Willebrand factor (vWF) and other plasma protein caused the initiation of platelet adhesion. Circulating platelets can bind to vWF through their GPIb-V-IX receptor and lead to the activation cascade [130].

Hemolysis rate was not affected by adding RE elements, indicating the release rate of those RE elements was very slow and didn't reach the threshold causing severe red blood cell lysis. In fact, the hemolysis rate of R1 and R2 was even lower than that of pure Mg. The hemolysis effect was most likely caused by the degradation of Mg, and subsequent increased osmosis pressure and elevated *p*H level.

Re-endothelialization on stent material surface has been suggested to be the key to reduce platelet adhesion, stent thrombosis and other adverse outcomes [70,131]. It was shown that increased endothelial coverage could significantly improve the long-term patency and reduce the interaction of blood components with artificial implants [9,132,133]. Some studies used L-929 and MG63 cells to test the biocompatibility of Mg alloys [30,34]. Little was known about how endothelial cells would interact with Mg alloys. In this study, Indirect MTT showed that there was a decreased cell viability tendency in all groups as the increase of concentrations of extract solutions. This was most likely due to the higher *p*H level and degradation products, leading to

mitochondrial oxidative stress. It is also interesting that no further decrease in viability were observed for R1 and R2 on days 4 and 7. In R3 and R4, cell viabilities through all the seven days were not significantly different from pure Mg, which indicated the release of REs from these two alloys didn't affect the HAECs viability. In addition, *Figure 14* shows even on the 7th day, more than half of the cells were still in healthy morphology, which seems to contradict with the 7th day MTT test. One possible explanation is that extract solution did not cause lethal damage to cell membranes or genetic substances but only lead to decreased enzymatic activities or altered gene regulation.

In direct cell attachment test, R1 and R2 had the lowest density of attached cells after 3 h indicating the surface of those materials were least favorable for cell adhesion and attachment. This is most likely caused by the combination effect of the presence of Dy and relative higher degradation rate compared with R3 and R4. As the degradation of R1 and R2 in ECM, Dy ions may inhibit the attachment of endothelial cells at the initial stage. Also, some swollen cells with green color were present on R1 and R2 indicating cells were dying though the cell membranes were still intact, therefore, retaining the green fluorescence. R3 had the comparable cell attachment and viability with the tissue culture plate control while R4 and pure Mg had moderate cell attachment. After 24 hours of incubation, most cells were dead on pure Mg and many gas bubbles emerged. A few live cells could still be observed on R1 and R2, but obviously in stressed conditions. In contrast, fully spread cells were the major population on R3 and R4 surfaces but the densities were much smaller than that on tissue culture plate. The death of cells could be mainly caused by increased *p*H value as the degradation of Mg alloys progressed. Results demonstrated that all Mg-RE alloys exhibited better endothelialization than pure Mg control in the static culture environment. It would be totally different in dynamic system or in

vivo, and we expect that endothelial cells would have much better attachment, survival and growth in vivo as the dynamic circulation system will remove the degradation products and prevent the hike of local *p*H.

5.1.3 Collagen self-assembly on Mg and subsequent cell attachment. Collagen, the ubiquitous ECM component, is a large family of triple-helical proteins. So far, around 28 types of collagen have been identified. Among them, type I collagen is the most abundant .It forms the backbone of ECM in a lot of tissues such as bone, dermis, and tendon. 90 % of the organic weight of bone is made up of type I collagen [134]. Type I collagen triple helix is composed of heterotrimer of two identical α1(I) chains and one α2(I) chain. Procollagen molecule is synthesized inside cells followed by post-translational modifications and then assembles into triple helix procollagen with diameter of 1.5 nm and length of 300 nm [134]. Then it is secreted to extracellular space by secretory vesicles and further processed by different proteinases. In vitro, collagen fibrils are formed by self-assembly into cross-striated fibrils with the characteristic D-period of 67 nm [135]. In natural bone tissues, collagen fibrils are the scaffold for biomineralization. It is believed that collagen molecules are secreted as amorphous and non-crystalline forms and then transformed into crystalline forms gradually [136].

Mg-based alloys have promising future for orthopedic applications with respect to their mechanical properties, degradation properties, and biocompatibility. While the exact mechanism of collagen fibril formation on Mg surface in vivo remains unknown, in vitro self-assembly model established in this work provides a simple and alternative way to study how Mg materials interact with collagen molecules.

Collagen fibril formation on mica surface involves the adsorption of collagen molecules, surface diffusion, nucleation of fibrils and fibril elongation [137,138]. A lot of studies have

shown that collagen could self-assemble into axially aligned fibrils with D-period similar to native bone tissues [139,140]. However, the assembly of collagen on mica surface could be different from that on Mg-alloy surface due to their distinct surface characteristics and electrostatics. Once in contact with body fluid, the metal elements in Mg materials will be oxidized into metal cations followed by the formation of a layer of metal hydroxide [8]. Metal ion would be released to the fluid during the degradation process and biomacromolecules such as protein, proteoglycan, and glycoprotein can be absorbed to the metal hydroxide layer [8]. It is interesting that for both pure Mg and AZ31 with different surface roughness, Mg ion released to the collagen solution after 2 h incubation didn't show significant difference. This is most likely due to the small total volume of solution (50 μl) and Mg ion was already saturated in the solution. At neutral *p*H, this metal hydrochloride layer is beneficial for collagen molecule adsorption since collagen molecule is positively charged. The absence of large fibril at low concentration of collagen monomer is most likely caused by the decreased chance for fibril nucleation. The concentration of collagen monomer can also affect the fibril growth rate and single fibrils grow independent from each other until they fuse with adjacent fibrils [137]. In addition, it was shown by Wang et al. that at low concentration collagen monomers form agglomerates in solution containing excessive Mg ions [141]. Similar agglomerates structure was also observed here on pure Mg and AZ31 surface at low collagen concentration. This might be caused by the high Mg^{2+}/collagen ratio and excessive Mg^{2+} could bind to collagen side chain leading to the increase of protein hydrophobicity and the dehydration of collagen [142]. Besides the release of metal ions, *p*H change accompanying the degradation process is another important factor that could affect collagen assembly. In the absence of other electrolytes, the isoelectric point (pI) of collagen is around 9.3 [143]. When *p*H approximates pI, the surface charge of

collagen monomers is decreased resulting in minimized electrostatic repulsion and better fibril assembly. This is supported by our data (*Figure 18*) where collagen fibrils loosely aligned at *p*H of 7 while they formed a dense layer of sheet at *p*H 9. As *p*H increased to 11, negatively charged collagen monomers could inhibit the nucleation of collagen fibril as well as the further attachment to Mg hydroxide layer. With the increase of incubation time to 8 h, small collagen fibrils could merge with adjacent fibrils forming thicker fibers (*Figure 19*C and *Figure 19*D). It is interesting to see that in almost all experiments, spherical particles with different size attached to collagen fibrils irrespective of the diameter of collagen fibrils. The shape and size of those particles are very similar to the mineral nucleation reported by Ferreia et al [144].

It is well documented that implant surface roughness alters osteoblast proliferation, differentiation, and extracellular matrix production [145]. Mendonca et al. showed that rough surface topography can stimulate collagen biosynthesis and accumulation on titanium [146]. Mg materials with RS have relative larger surface area that increases the chance of collagen molecules adsorption. This is probably why the amount of collagen absorbed on the RS and SR materials was significantly higher than that on materials with SS. Also, surface energy could affect collagen adsorption and structural rearrangement. It is noticeable that the amount of absorbed collagen decreased at 8 h on the materials with RS and SR. This phenomenon is most likely caused by severe pitting corrosion on rougher surface compared with smoother surface [147,148]. In addition, surface roughness not only affected the amount of collagen absorbed but also the structure of the fibrils. The slight morphological difference of collagen fibrils on Mg and AZ31 is likely caused by the presence of Zn^{2+} and Al^{3+}, the AZ31 degradation products [143].

Enhanced cell attachment on the materials with SS is consistent with previous studies [149]. On AZ31 material, a lot of dead cells could be observed on the RS materials after the first

day. This is most likely due to the failure of cell attachment or hampered cell attachment on the RS where cells could only anchor themselves at reduced area caused by the existence of the grooves and ridges. The grooves and ridges showed contact guidance effect on cell alignment. It was demonstrated before that the tip of filopodia most likely attaches to the top of the ridges [150]. During cell migration, it would be much easier for cell to move the tip of the adhesion along the ridge than to move the tip of the adhesion perpendicular to the direction of ridges. That may be the reason why cells on the rough surface materials all aligned parallel to the direction of ridges. Cells showed similar proliferation results on AZ31 with different surface roughness indicating that surface roughness and collagen structure will not affect cell proliferation. However, cells did not show similar proliferation result on pure Mg at 4^{th} day and 7^{th} day. Cell density significantly decreased at the Mg with RS and SR. Healthy spreading cells could hardly be found on the SS pure Mg materials. At body temperature, melting time for human type I collagen is around several days [151]. Compared with AZ31, the relative faster degradation rate of pure Mg could lead to higher concentration of degradation products and higher *p*H in solution, which might accelerate dissociation of attached collagen and cause decreased cell density. In addition, the thick collagen ribbon structure doesn't resemble native collagen structure in bone. The collagen fibrils in *Figure 21*C and *Figure 21*D showed high similarity with the demineralized circumferential lamellar bone [152]. Ideally, the preferable orthopedic implants should not only be able to stimulate bone cell growth but also to support the assembly of collagen monomer into native fibrils at the bone-implant interface.

This in vitro model was developed to mimic the in vivo interactions between collagen and the Mg implant at the interface. It provided useful information on the molecular mechanism of such an interaction that will influence the fate of the implant. However, limitations do exist in

this study . For example, different cell regulations and other protein interactions were neglected. Other types of bone cells and non-collagenous proteins also play important roles in collagen assembly [153]. Therefore, future studies are needed to address these factors. Specifically, one topic could be to investigate how mineralization happens around the interfaces.

5.1.4 Endothelialization of Mg-RE alloys with fluoride conversion coating. Previous studies have shown that fluoride conversion coating can improve the corrosion resistance of Mg materials [57,154-157]. Fluorine is essential for human dental development. Mao et al. showed, that Mg-Nd-Zn-Zr alloy, after treated with HF solution for 12 hours, forms a porous layer of MgF_2 on its surface [57]. It was shown that the bonding strength of interlayer of MgF_2 in pure Mg treated with HF was found to be 34 MPa [158]. Wan et al. also reported a super-hydrophobic porous surface created by 1% HF treatment [67]. It is believed that the porous structure played an important role in trapping air, which leads to the hydrophobic surface. The porous structure with smaller cavities was observed in *Figure 27*. MgF_2 is insoluble in water and the small cavities among the granular structure were able to trap air. The capability of the HF modified layer to ameliorate Mg degradation is mainly dependent on the size of those granular structures. The smaller cavities on the MgF_2 layer, the more efficient they were at trapping air.

Another consideration is that MgF_2 layer on the material surface might be brittle according to a previous study [159], thus a modification of the mechanical properties has to be expected. Therefore, one need be cautious when applying this HF treatment for balloon expandable stent materials.

Direct endothelialization showed that HF treatment could improve endothelial cell attachment and proliferation compared with bare material and collagen coated material. Collagen coating was used as positive control in this study since it is the most abundant extracellular

matrix protein which provides adhesion points for cell attachment and migration. Ao et al. showed that type I collagen covalently combined with titanium enhanced cell-material interactions and improved hMSC attachment, proliferation, and differentiation [160]. In addition, Collagen-coated Ti could promote expression of osteoblast phenotype and enhance bone formation around the implants [161]. However, on Mg surface collagen coating didn't show much improvement for HCAECs attachment and proliferation. This is probably due to the different corrosion rate and corrosion mechanism. As the degradation of Mg alloys progressed, increased *p*H and excess alloying element ions could affect the 3-D structure of biomolecules, leading to the failure of recognition between extracellular matrix proteins and the cell membrane receptors. In addition, hydrogen gas production during the corrosion process could form gas bubbles on the Mg surface, which may have prevented both biomacromolecule attachment and cell adhesion.

5.2 Future Research

The cytocompatibility of Mg material degradation products on endothelial cell, hemocompatibility and endothelialization of Mg-RE alloys, collage self-assembly on bone orthopedic materials and the endothelializition on fluoride conversion coating Mg materials was studied in this research project. The findings from this study provide useful information on cell-metal ion interaction and preliminary safety evaluation of Mg-based stent material. Also, Mg alloying with REs and HF conversion coating could significantly improve the endothelial cell attachment in vitro showing great potential for clinical application. However, limitations do exist in each of the studies and there are several aspects that should be address in the future. The degradation products from stent material are the combination of all the metal elements instead of the single metal ion tested in this research. Therefore, to study how the mixture of Mg

degradation products affects cytocompatibility will be the next step for evaluating material toxicity in vitro. The effect of other factors such as *p*H change, air bubble formations and metal debris accompanying the degradation process on cell behavior should also be considered. In addition, it is also very important to study how those factors affect smooth muscle cell and blood cells.

The endotheliallization experiments were carried out in a static environment. However, *in vivo*, both endothelial cells and stent materials are subjected to blood flow. For this reason, static endothelialization does not represent the same endothelial behavior or degradation propertied of Mg stent exposed to blood flow and it is important to simulate the flow condition for endothelial attachment experiment. For the HF conversion coating, future research should elucidate the degradation mechanism of MgF_2. What kind of finial degradation products this MgF_2 layer will produce and how are those degradation products metabolized by cells? Is there any long-term toxic effect of fluorine? Those questions should all be answered before the application of HF coating on stent material. In the collagen self-assembly on bone orthopedic materials, future work should also include how other molecules in bone tissues, such as some non-collagenous glycoproteins, hyaluronic acid, chondroitin sulfate and mineral deposition interact with Mg materials. Besides, it is also unknown how Mg interacts with osteoblasts, osteoclasts and osteocytes. Those studies would further provide useful information to evaluate Mg-based orthopedic materials and stent materials.

References

1. Puleo D, Nanci A (1999) Understanding and controlling the bone–implant interface. Biomaterials 20: 2311-2321.

2. Place ES, Evans ND, Stevens MM (2009) Complexity in biomaterials for tissue engineering. Nature materials 8: 457-470.

3. Rabkin E, Schoen FJ (2002) Cardiovascular tissue engineering. Cardiovascular pathology 11: 305-317.

4. Heydarkhan-Hagvall S, Esguerra M, Helenius G, Söderberg R, Johansson BR, et al. (2006) Production of extracellular matrix components in tissue-engineered blood vessels. Tissue Eng 12: 831-842.

5. Solan A, Prabhakar V, Niklason L. Engineered vessels: importance of the extracellular matrix; 2001. Elsevier. pp. 66-68.

6. Niklason L, Gao J, Abbott W, Hirschi K, Houser S, et al. (1999) Functional arteries grown in vitro. Science 284: 489-493.

7. Zhao N, Watson N, Xu Z, Chen Y, Waterman J, et al. (2014) In Vitro Biocompatibility and Endothelialization of Novel Magnesium-Rare Earth Alloys for Improved Stent Applications. PloS one 9: e98674.

8. Zheng Y, Gu X, Witte F (2014) Biodegradable metals. Materials Science and Engineering: R: Reports 77: 1-34.

9. Zheng WT, Wang ZH, Song LJ, Zhao Q, Zhang J, et al. (2012) Endothelialization and patency of RGD-functionalized vascular grafts in a rabbit carotid artery model. Biomaterials 33: 2880-2891.

10. Peuster M, Wohlsein P, Brügmann M, Ehlerding M, Seidler K, et al. (2001) A novel approach to temporary stenting: degradable cardiovascular stents produced from corrodible metal—results 6–18 months after implantation into New Zealand white rabbits. Heart 86: 563-569.

11. Zartner P, Cesnjevar R, Singer H, Weyand M (2005) First successful implantation of a biodegradable metal stent into the left pulmonary artery of a preterm baby. Catheterization and Cardiovascular Interventions 66: 590-594.

12. Staiger MP, Pietak AM, Huadmai J, Dias G (2006) Magnesium and its alloys as orthopedic biomaterials: a review. Biomaterials 27: 1728-1734.

13. Witte F, Kaese V, Haferkamp H, Switzer E, Meyer-Lindenberg A, et al. (2005) In vivo corrosion of four magnesium alloys and the associated bone response. Biomaterials 26: 3557-3563.

14. Choudhary L, Singh Raman R (2012) Magnesium alloys as body implants: Fracture mechanism under dynamic and static loadings in a physiological environment. Acta Biomater 8: 916-923.

15. Staiger MP, Pietak AM, Huadmai J, Dias G (2006) Magnesium and its alloys as orthopedic biomaterials: a review. Biomaterials 27: 1728-1734.

16. Zhao N, Zhu D (2013) Application of Mg–based alloys for cardiovascular stents. International Journal of Biomedical Engineering and Technology 12: 382-398.

17. Witte F, Kaese V, Haferkamp H, Switzer E, Meyer-Lindenberg A, et al. (2005) In vivo corrosion of four magnesium alloys and the associated bone response. Biomaterials 26: 3557-3563.

18. Xu L, Yu G, Zhang E, Pan F, Yang K (2007) In vivo corrosion behavior of Mg-Mn-Zn alloy for bone implant application. Journal of Biomedical Materials Research Part A 83: 703-711.

19. Castellani C, Lindtner RA, Hausbrandt P, Tschegg E, Stanzl-Tschegg SE, et al. (2011) Bone–implant interface strength and osseointegration: biodegradable magnesium alloy versus standard titanium control. Acta Biomaterialia 7: 432-440.

20. Gill P, Munroe N (2012) Review on magnesium alloys as biodegradable implant materials. International Journal of Biomedical Engineering and Technology 10: 383-398.

21. Troitskii V, Tsitrin D (1944) The resorbing metallic alloy 'Osteosinthezit'as material for fastening broken bone. Khirurgiia 8: 41-44.

22. Witte F (2010) The history of biodegradable magnesium implants: a review. Acta Biomaterialia 6: 1680-1692.

23. Yang Z, Li J, Zhang J, Lorimer G, Robson J (2008) Review on research and development of magnesium alloys. Acta Metallurgica Sinica (English Letters) 21: 313-328.

24. YOKEL RA (2000) The Toxicology of Aluminum. Neurotoxicology 21: 813-828.

25. Zhang E, Yin D, Xu L, Yang L, Yang K (2009) Microstructure, mechanical and corrosion properties and biocompatibility of Mg–Zn–Mn alloys for biomedical application. Materials Science and Engineering: C 29: 987-993.

26. Ye C, Zheng Y, Wang S, Xi T, Li Y (2012) In vitro corrosion and biocompatibility study of phytic acid modified WE43 magnesium alloy. Applied Surface Science 258: 3420-3427.

27. Srinivasan A, Ranjani P, Rajendran N (2012) Electrochemical polymerization of Pyrrole over AZ31 Mg alloy for biomedical applications. Electrochimica Acta.

28. Gu X, Zheng Y, Cheng Y, Zhong S, Xi T (2009) In vitro corrosion and biocompatibility of binary magnesium alloys. Biomaterials 30: 484-498.

29. Hanzi AC, Gerber I, Schinhammer M, Loffler JF, Uggowitzer PJ (2010) On the in vitro and in vivo degradation performance and biological response of new biodegradable Mg-Y-Zn alloys. Acta Biomater 6: 1824-1833.

30. Yan T, Tan L, Xiong D, Liu X, Zhang B, et al. (2010) Fluoride treatment and in vitro corrosion behavior of an AZ31B magnesium alloy. Materials Science and Engineering: C 30: 740-748.

31. Liu C, Xin Y, Tang G, Chu PK (2007) Influence of heat treatment on degradation behavior of bio-degradable die-cast AZ63 magnesium alloy in simulated body fluid. Materials Science and Engineering: A 456: 350-357.

32. Seuss F, Seuss S, Turhan M, Fabry B, Virtanen S (2011) Corrosion of Mg alloy AZ91D in the presence of living cells. Journal of Biomedical Materials Research Part B: Applied Biomaterials 99: 276-281.

33. Bornapour M, Muja N, Shum-Tim D, Cerruti M, Pekguleryuz M (2013) Biocompatibility and biodegradability of Mg-Sr alloys: the formation of Sr-substituted hydroxyapatite. Acta Biomater 9: 5319-5330.

34. Gu X, Zheng Y, Zhong S, Xi T, Wang J, et al. (2010) Corrosion of, and cellular responses to Mg–Zn–Ca bulk metallic glasses. Biomaterials 31: 1093-1103.

35. Zhou WR, Zheng YF, Leeflang MA, Zhou J (2013) Mechanical property, biocorrosion and in vitro biocompatibility evaluations of Mg-Li-(Al)-(RE) alloys for future cardiovascular stent application. Acta Biomater 4: 00047-00040.

36. Zhang X, Yuan G, Mao L, Niu J, Fu P, et al. (2012) Effects of extrusion and heat treatment on the mechanical properties and biocorrosion behaviors of a Mg–Nd–Zn–Zr alloy. Journal of the Mechanical Behavior of Biomedical Materials 7: 77-86.

37. Mao L, Yuan G, Wang S, Niu J, Wu G, et al. (2012) A novel biodegradable Mg–Nd–Zn–Zr alloy with uniform corrosion behavior in artificial plasma. Materials Letters.

38. Hou S, Zhang R, Guan S, Ren C, Gao J, et al. (2012) In vitro corrosion behavior of Ti-O film deposited on fluoride-treated Mg–Zn–Y–Nd alloy. Applied Surface Science 258: 3571-3577.

39. Xu S, Oh-Ishi K, Kamado S, Uchida F, Homma T, et al. (2011) High-strength extruded Mg–Al–Ca–Mn alloy. Scripta Materialia 65: 269-272.

40. Perez P, Onofre E, Cabeza S, Llorente I, del Valle JA, et al. (2013) Corrosion behaviour of Mg-Zn-Y-Mischmetal alloys in phosphate buffer saline solution. Corrosion Science 69: 226-235.

41. Geis-Gerstorfer J, Schille C, Schweizer E, Rupp F, Scheideler L, et al. (2011) Blood triggered corrosion of magnesium alloys. Materials Science and Engineering B-Advanced Functional Solid-State Materials 176: 1761-1766.

42. Hou S, Mi L, Wang L, Zhu S, Hu J, et al. (2013) Corrosion protection of Mg-Zn-Y-Nd alloy by flower-like nanostructured TiO2 film for vascular stent application. Journal of Chemical Technology and Biotechnology.

43. Ji DW, Liu CM, Chen ZY, Wang HH, Wang B (2013) Effects of Zn content on microstructures and mechanical properties of as cast Mg-Zn-Y-Zr alloys. Materials Science and Technology 29: 480-486.

44. Nam SW, Kim WT, Kim DH, Kim TS (2013) Microstructure and corrosion behavior of rapidly solidified Mg-Zn-Y alloys. Metals and Materials International 19: 205-209.

45. Wang Z, Huang YD, Srinivasan A, Liu Z, Beckmann F, et al. (2013) Hot tearing susceptibility of binary Mg-Y alloy castings. Materials & Design 47: 90-100.

46. Seitz JM, Eifler R, Stahl J, Kietzmann M, Bach FW (2012) Characterization of MgNd2 alloy for potential applications in bioresorbable implantable devices. Acta Biomaterialia 8: 3852-3864.

47. Fan J, Qiu X, Niu X, Tian Z, Sun W, et al. (2013) Microstructure, mechanical properties, in vitro degradation and cytotoxicity evaluations of Mg-1.5 Y-1.2 Zn-0.44 Zr alloys for biodegradable metallic implants. Materials Science and Engineering: C.

48. Feyerabend F, Fischer J, Holtz J, Witte F, Willumeit R, et al. (2010) Evaluation of short-term effects of rare earth and other elements used in magnesium alloys on primary cells and cell lines. Acta Biomaterialia 6: 1834-1842.

49. Wu Q, Zhu S, Wang L, Liu Q, Yue G, et al. (2012) The microstructure and properties of cyclic extrusion compression treated Mg–Zn–Y–Nd alloy for vascular stent application. Journal of the Mechanical Behavior of Biomedical Materials 8: 1-7.

50. Ge Q, Dellasega D, Demir AG, Vedani M (2013) The processing of ultrafine-grained Mg tubes for biodegradable stents. Acta Biomaterialia.

51. Itoi T, Inazawa T, Yamasaki M, Kawamura Y, Hirohashi M (2013) Microstructure and mechanical properties of Mg-Zn-Y alloy sheet prepared by hot-rolling. Materials Science and Engineering a-Structural Materials Properties Microstructure and Processing 560: 216-223.

52. Gu X, Zhou W, Zheng Y, Cheng Y, Wei S, et al. (2010) Corrosion fatigue behaviors of two biomedical Mg alloys–AZ91D and WE43–in simulated body fluid. Acta Biomaterialia 6: 4605-4613.

53. Avedesian MM, Baker H (1999) ASM specialty handbook: magnesium and magnesium alloys. ASM international 274.

54. Drynda A, Hassel T, Hoehn R, Perz A, Bach FW, et al. (2010) Development and biocompatibility of a novel corrodible fluoride-coated magnesium-calcium alloy with improved degradation kinetics and adequate mechanical properties for cardiovascular applications. J Biomed Mater Res A 93: 763-775.

55. Wang H, Guan S, Wang X, Ren C, Wang L (2010) In vitro degradation and mechanical integrity of Mg–Zn–Ca alloy coated with Ca-deficient hydroxyapatite by the pulse electrodeposition process. Acta Biomaterialia 6: 1743-1748.

56. Wang B, Guan SK, Wang J, Wang LG, Zhu SJ (2011) Effects of Nd on microstructures and properties of extruded Mg-2Zn-0.46Y-xNd alloys for stent application. Materials Science and Engineering B-Advanced Functional Solid-State Materials 176: 1673-1678.

57. Mao L, Yuan GY, Niu JL, Zong Y, Ding WJ (2013) In vitro degradation behavior and biocompatibility of Mg-Nd-Zn-Zr alloy by hydrofluoric acid treatment. Materials Science & Engineering C-Materials for Biological Applications 33: 242-250.

58. Li J, Cao P, Zhang X, Zhang S, He Y (2010) In vitro degradation and cell attachment of a PLGA coated biodegradable Mg–6Zn based alloy. Journal of Materials Science 45: 6038-6045.

59. Hehrlein C, Zimmermann M, Metz J, Ensinger W, Kübler W (1995) Influence of surface texture and charge on the biocompatibility of endovascular stents. Coronary Artery Disease 6: 581.

60. Heldman AW, Cheng L, Jenkins GM, Heller PF, Kim D-W, et al. (2001) Paclitaxel stent coating inhibits neointimal hyperplasia at 4 weeks in a porcine model of coronary restenosis. Circulation 103: 2289-2295.

61. Nakayama Y, Ji-Youn K, Nishi S, Ueno H, Matsuda T (2001) Development of high-performance stent: Gelatinous photogel-coated stent that permits drug delivery and gene transfer. J Biomed Mater Res 57: 559-566.

62. Huang Y, Wang L, Verweire I, Qiang B, Liu X, et al. (2002) Optimization of local methylprednisolone delivery to inhibit inflammatory reaction and neointimal hyperplasia of coated coronary stents. J Invasive Cardiol 14: 505-513.

63. Thierry B, Winnik FM, Merhi Y, Silver J, Tabrizian M (2004) Radionuclides-hyaluronan-conjugate thromboresistant coatings to prevent in-stent restenosis. Biomaterials 25: 3895-3905.

64. Chen M-C, Liang H-F, Chiu Y-L, Chang Y, Wei H-J, et al. (2005) A novel drug-eluting stent spray-coated with multi-layers of collagen and sirolimus. Journal of controlled release 108: 178-189.

65. Huang N, Leng Y, Yang P, Chen J, Sun H, et al. (2006) Surface modification of coronary artery stent by Ti–O/Ti–N complex film coating prepared with plasma immersion ion implantation and deposition. Nuclear Instruments and Methods in Physics Research Section B: Beam Interactions with Materials and Atoms 242: 18-21.

66. Liu C, Chu PK, Lin G, Qi M (2006) Anti-corrosion characteristics of nitride-coated AISI 316L stainless steel coronary stents. Surface and Coatings Technology 201: 2802-2806.

67. Wan P, Wu J, Tan L, Zhang B, Yang K (2013) Research on super-hydrophobic surface of biodegradable magnesium alloys used for vascular stents. Mater Sci Eng C Mater Biol Appl 33: 2885-2890.

68. Chen Y, Song Y, Zhang S, Li J, Zhao C, et al. (2011) Interaction between a high purity magnesium surface and PCL and PLA coatings during dynamic degradation. Biomedical Materials 6: 025005.

69. Wang J, He Y, Maitz MF, Collins B, Xiong K, et al. (2013) A surface-eroding poly (1, 3-trimethylene carbonate) coating for fully-biodegradable magnesium-based stent applications: toward better biofunction, biodegradation, and biocompatibility. Acta Biomaterialia.

70. Xiao X, Yu H, Zhu Q, Li G, Qu Y, et al. (2013) In Vivo Corrosion Resistance of Ca-P Coating on AZ60 Magnesium Alloy. Journal of Bionic Engineering 10: 156-161.

71. Zhang XB, Yuan GY, Fang XX, Wang ZZ, Zhang T (2013) Effects of solution treatment on yield ratio and biocorrosion behaviour of as-extruded Mg-2.7Nd-0.2Zn-0.4Zr alloy for cardiovascular stent application. Materials Technology 28: 155-158.

72. Wang Y, Guo J, Shao Z, Zhuang J, Jin M, et al. (2013) A metasilicate-based ceramic coating formed on magnesium alloy by microarc oxidation and its corrosion in simulated body fluid. Surface and Coatings Technology.

73. Yue T, Huang K (2011) Laser Forming of Zr-Based Coatings on AZ 91 D Magnesium Alloy Substrates for Wear and Corrosion Resistance Improvement. Materials transactions 52: 810-813.

74. Spencer K, Zhang M-X (2009) Heat treatment of cold spray coatings to form protective intermetallic layers. Scripta Materialia 61: 44-47.

75. Weyermann J, Lochmann D, Zimmer A (2005) A practical note on the use of cytotoxicity assays. International journal of pharmaceutics 288: 369-376.

76. Sternberg K, Gratz M, Koeck K, Mostertz J, Begunk R, et al. (2012) Magnesium used in bioabsorbable stents controls smooth muscle cell proliferation and stimulates endothelial cells in vitro. J Biomed Mater Res B Appl Biomater 100: 41-50.

77. YE C-h, XI T-f, ZHENG Y-f, WANG S-q, LI Y-d (2013) In vitro corrosion and biocompatibility of phosphating modified WE43 magnesium alloy. Transactions of Nonferrous Metals Society of China 23: 996-1001.

78. Zhang S, Zhang X, Zhao C, Li J, Song Y, et al. (2010) Research on an Mg–Zn alloy as a degradable biomaterial. Acta Biomaterialia 6: 626-640.

79. Li H, Zhong H, Xu K, Yang K, Liu J, et al. (2011) Enhanced efficacy of sirolimus-eluting bioabsorbable magnesium alloy stents in the prevention of restenosis. J Endovasc Ther 18: 407-415.

80. Erbel R, Di Mario C, Bartunek J, Bonnier J, de Bruyne B, et al. (2007) Temporary scaffolding of coronary arteries with bioabsorbable magnesium stents: a prospective, non-randomised multicentre trial. The Lancet 369: 1869-1875.

81. Ghimire G, Spiro J, Kharbanda R, Roughton M, Barlis P, et al. (2009) Initial evidence for the return of coronary vasoreactivity following the absorption of bioabsorbable magnesium alloy coronary stents. EuroIntervention: journal of EuroPCR in collaboration with the Working Group on Interventional Cardiology of the European Society of Cardiology 4: 481.

82. Waksman R, Erbel R, Di Mario C, Bartunek J, de Bruyne B, et al. (2009) Early- and long-term intravascular ultrasound and angiographic findings after bioabsorbable magnesium stent implantation in human coronary arteries. JACC Cardiovasc Interv 2: 312-320.

83. Di Mario C, Griffiths H, Goktekin O, Peeters N, Verbist J, et al. (2004) Drug-Eluting Bioabsorbable Magnesium Stent. Journal of interventional cardiology 17: 391-395.

84. Li HW, Zhong HS, Xu K, Yang K, Liu J, et al. (2011) Enhanced Efficacy of Sirolimus-Eluting Bioabsorbable Magnesium Alloy Stents in the Prevention of Restenosis. Journal of Endovascular Therapy 18: 407-415.

85. Heublein B, Rohde R, Kaese V, Niemeyer M, Hartung W, et al. (2003) Biocorrosion of magnesium alloys: a new principle in cardiovascular implant technology? Heart 89: 651-656.

86. Haude M, Erbel R, Erne P, Verheye S, Vermeersch P, et al. (2012) TCT-38 Two-Year Clinical Data Of Cohort 1 And Multi-Modality Imaging Results Up To 1-Year Follow-Up Of The BIOSOLVE-I Study With The Paclitaxel-Eluting Bioabsorbable Magnesium Scaffold (DREAMS). Journal of the American College of Cardiology 60.

87. Haude M, Erbel R, Erne P, Verheye S, Degen H, et al. (2013) Safety and performance of the drug-eluting absorbable metal scaffold (DREAMS) in patients with de-novo coronary lesions: 12 month results of the prospective, multicentre, first-in-man BIOSOLVE-I trial. Lancet 381: 836-844.

88. Lim GB (2013) Interventional cardiology: DREAMS of a bioabsorbable stent coming true. Nature Reviews Cardiology.

89. Xu Z, Smith C, Chen S, Sankar J (2011) Development and microstructural characterizations of Mg–Zn–Ca alloys for biomedical applications. Materials Science and Engineering: B 176: 1660-1665.

90. ISO E (2008) 10993-12: 2008–Biological evaluation of medical devices–Part 12: Sample preparation and reference materials (ISO 10993-12: 2007). German version: DIN EN ISO: 10993-10912.

91. Standard A (2006) G102-89, Standard Practice for Calculation of Corrosion Rates and Related Information from Electrochemical Measurements. Annual Book of ASTM Standards, ASTM International, West Conshohocken, PA 3.

92. Livak KJ, Schmittgen TD (2001) Analysis of Relative Gene Expression Data Using Real-Time Quantitative PCR and the 2− ΔΔCT Method. methods 25: 402-408.

93. Kim HW, Li LH, Lee EJ, Lee SH, Kim HE (2005) Fibrillar assembly and stability of collagen coating on titanium for improved osteoblast responses. Journal of Biomedical Materials Research Part A 75: 629-638.

94. Ao H, Xie Y, Tan H, Yang S, Li K, et al. (2013) Fabrication and in vitro evaluation of stable collagen/hyaluronic acid biomimetic multilayer on titanium coatings. Journal of The Royal Society Interface 10.

95. Chen X, Ergun A, Gevgilili H, Ozkan S, Kalyon DM, et al. (2013) Shell-core bi-layered scaffolds for engineering of vascularized osteon-like structures. Biomaterials 34: 8203-8212.

96. Wu L, Luthringer BJ, Feyerabend F, Schilling AF, Willumeit R (2014) Effects of extracellular magnesium on the differentiation and function of human osteoclasts. Acta Biomaterialia 10: 2843-2854.

97. Tojkander S, Gateva G, Lappalainen P (2012) Actin stress fibers–assembly, dynamics and biological roles. Journal of cell science 125: 1855-1864.

98. Zhang S, Li J, Song Y, Zhao C, Zhang X, et al. (2009) In vitro degradation, hemolysis and MC3T3-E1 cell adhesion of biodegradable Mg–Zn alloy. Materials Science and Engineering: C 29: 1907-1912.

99. Anderson JM (2001) Biological responses to materials. Annual Review of Materials Research 31: 81-110.

100. Sumpio BE, Timothy Riley J, Dardik A (2002) Cells in focus: endothelial cell. The international journal of biochemistry & cell biology 34: 1508-1512.

101. Fischer J, Pröfrock D, Hort N, Willumeit R, Feyerabend F (2011) Improved cytotoxicity testing of magnesium materials. Materials Science and Engineering: B 176: 1773-1777.

102. Zhang J, Kong N, Shi Y, Niu J, Mao L, et al. (2014) Influence of proteins and cells on in vitro corrosion of Mg-Nd-Zn-Zr alloy. Corrosion Science: In press.

103. Song W, Zhang J, Guo J, Zhang J, Ding F, et al. (2010) Role of the dissolved zinc ion and reactive oxygen species in cytotoxicity of ZnO nanoparticles. Toxicology letters 199: 389-397.

104. Sammalkorpi M, Karttunen M, Haataja M (2009) Ionic surfactant aggregates in saline solutions: sodium dodecyl sulfate (SDS) in the presence of excess sodium chloride (NaCl) or calcium chloride (CaCl2). The Journal of Physical Chemistry B 113: 5863-5870.

105. Drynda A, Deinet N, Braun N, Peuster M (2009) Rare earth metals used in biodegradable magnesium-based stents do not interfere with proliferation of smooth muscle cells but do

induce the upregulation of inflammatory genes. Journal of Biomedical Materials Research Part A 91: 360-369.

106. Lozano RM, Pérez-Maceda BT, Carboneras M, Onofre-Bustamante E, García-Alonso MC, et al. (2013) Response of MC3T3-E1 osteoblasts, L929 fibroblasts, and J774 macrophages to fluoride surface-modified AZ31 magnesium alloy. Journal of Biomedical Materials Research Part A 101: 2753-2762.

107. Brar HS, Ball JP, Berglund IS, Allen JB, Manuel MV (2013) A study of a biodegradable Mg–3Sc–3Y alloy and the effect of self-passivation on the in vitro degradation. Acta biomaterialia 9: 5331-5340.

108. Berglund IS, Brar HS, Dolgova N, Acharya AP, Keselowsky BG, et al. (2012) Synthesis and characterization of Mg-Ca-Sr alloys for biodegradable orthopedic implant applications. Journal of Biomedical Materials Research Part B: Applied Biomaterials 100: 1524-1534.

109. Han X, Gelein R, Corson N, Wade-Mercer P, Jiang J, et al. (2011) Validation of an LDH assay for assessing nanoparticle toxicity. Toxicology 287: 99-104.

110. Fischer J, Prosenc MH, Wolff M, Hort N, Willumeit R, et al. (2010) Interference of magnesium corrosion with tetrazolium-based cytotoxicity assays. Acta biomaterialia 6: 1813-1823.

111. Tsaryk R, Peters K, Barth S, Unger RE, Scharnweber D, et al. (2013) The role of oxidative stress in pro-inflammatory activation of human endothelial cells on Ti6Al4V alloy. Biomaterials 34: 8075-8085.

112. Horie M, Fujita K, Kato H, Endoh S, Nishio K, et al. (2012) Association of the physical and chemical properties and the cytotoxicity of metal oxide nanoparticles: metal ion release, adsorption ability and specific surface area. Metallomics 4: 350-360.

113. Cairns RA, Harris IS, Mak TW (2011) Regulation of cancer cell metabolism. Nature Reviews Cancer 11: 85-95.

114. Maier JA, Bernardini D, Rayssiguier Y, Mazur A (2004) High concentrations of magnesium modulate vascular endothelial cell behaviour in vitro. Biochimica et Biophysica Acta (BBA)-Molecular Basis of Disease 1689: 6-12.

115. Lamalice L, Le Boeuf F, Huot J (2007) Endothelial cell migration during angiogenesis. Circulation research 100: 782-794.

116. Pin A-L, Houle F, Fournier P, Guillonneau M, Paquet ÉR, et al. (2012) Annexin-1-mediated endothelial cell migration and angiogenesis are regulated by vascular endothelial growth factor (VEGF)-induced inhibition of miR-196a expression. Journal of Biological Chemistry 287: 30541-30551.

117. Alexander RA, Prager GW, Mihaly-Bison J, Uhrin P, Sunzenauer S, et al. (2012) VEGF-induced endothelial cell migration requires urokinase receptor (uPAR)-dependent integrin redistribution. Cardiovascular research 94: 125-135.

118. Banai S, Haggroth L, Epstein SE, Casscells W (1990) Influence of extracellular magnesium on capillary endothelial cell proliferation and migration. Circulation research 67: 645-650.

119. Dimmeler S, Dernbach E, Zeiher AM (2000) Phosphorylation of the endothelial nitric oxide synthase at ser-1177 is required for VEGF-induced endothelial cell migration. FEBS letters 477: 258-262.

120. Dejana E (2004) Endothelial cell–cell junctions: happy together. Nature Reviews Molecular Cell Biology 5: 261-270.

121. Soria G, Ben-Baruch A (2008) The inflammatory chemokines CCL2 and CCL5 in breast cancer. Cancer letters 267: 271-285.

122. Rubin H (2005) The membrane, magnesium, mitosis (MMM) model of cell proliferation control. Magnesium research 18: 268-274.

123. Sharif F, Hynes SO, Cooney R, Howard L, McMahon J, et al. (2008) Gene-eluting stents: adenovirus-mediated delivery of eNOS to the blood vessel wall accelerates re-endothelialization and inhibits restenosis. Molecular Therapy 16: 1674-1680.

124. McEver RP, Martin MN (1984) A monoclonal antibody to a membrane glycoprotein binds only to activated platelets. Journal of Biological Chemistry 259: 9799-9804.

125. Goodman S, Grasel T, Cooper S, Albrecht R (1989) Platelet shape change and cytoskeletal reorganization on polyurethaneureas. Journal of biomedical materials research 23: 105-123.

126. Serruys PW, Strauss BH, Beatt KJ, Bertrand ME, Puel J, et al. (1991) Angiographic follow-up after placement of a self-expanding coronary-artery stent. New England Journal of Medicine 324: 13-17.

127. Costa MA, Simon DI (2005) Molecular basis of restenosis and drug-eluting stents. Circulation 111: 2257-2273.

128. Inoue T, Node K (2009) Molecular basis of restenosis and novel issues of drug-eluting stents. Circulation journal: official journal of the Japanese Circulation Society 73: 615-621.

129. Hwang DL, Yen CF, Nadler JL (1992) Effect of extracellular magnesium on platelet activation and intracellular calcium mobilization. American journal of hypertension 5: 700-706.

130. Varga-Szabo D, Pleines I, Nieswandt B (2008) Cell adhesion mechanisms in platelets. Arterioscler Thromb Vasc Biol 28: 403-412.

131. Hiltunen MO, Laitinen M, Turunen MP, Jeltsch M, Hartikainen J, et al. (2000) Intravascular adenovirus-mediated VEGF-C gene transfer reduces neointima formation in balloon-denuded rabbit aorta. Circulation 102: 2262-2268.

132. Zhou M, Liu Z, Liu C, Jiang XF, Wei ZQ, et al. (2012) Tissue engineering of small-diameter vascular grafts by endothelial progenitor cells seeding heparin-coated decellularized scaffolds. Journal of Biomedical Materials Research Part B-Applied Biomaterials 100B: 111-120.

133. De Visscher G, Mesure L, Meuris B, Ivanova A, Flameng W (2012) Improved endothelialization and reduced thrombosis by coating a synthetic vascular graft with fibronectin and stem cell homing factor SDF-1 alpha. Acta Biomaterialia 8: 1330-1338.

134. Gelse K, Pöschl E, Aigner T (2003) Collagens—structure, function, and biosynthesis. Advanced drug delivery reviews 55: 1531-1546.

135. Kadler K, Holmes D, Trotter J, Chapman J (1996) Collagen fibril formation. Biochem J 316: 1-11.

136. Ferreira AM, Gentile P, Chiono V, Ciardelli G (2012) Collagen for bone tissue regeneration. Acta Biomaterialia 8: 3191-3200.

137. Cisneros DA, Hung C, Franz CM, Muller DJ (2006) Observing growth steps of collagen self-assembly by time-lapse high-resolution atomic force microscopy. Journal of structural biology 154: 232-245.

138. Narayanan B, Gilmer GH, Tao J, De Yoreo JJ, Ciobanu CV (2014) Self-assembly of collagen on surfaces: the interplay of collagen-collagen and collagen-substrate interactions. Langmuir 30: 1343-1350.

139. Loo RW, Goh MC (2008) Potassium ion mediated collagen microfibril assembly on mica. Langmuir 24: 13276-13278.

140. Leow WW, Hwang W (2011) Epitaxially guided assembly of collagen layers on mica surfaces. Langmuir 27: 10907-10913.

141. Wang L, Guo Y, Li P, Song Y (2014) Anion-Specific Effects on the Assembly of Collagen Layers Mediated by Magnesium Ion on Mica Surface. The Journal of Physical Chemistry B.

142. He L, Cai S, Wu B, Mu C, Zhang G, et al. (2012) Trivalent chromium and aluminum affect the thermostability and conformation of collagen very differently. Journal of inorganic biochemistry 117: 124-130.

143. Zhao N, Workman B, Zhu D (2014) Endothelialization of Novel Magnesium-Rare Earth Alloys with Fluoride and Collagen Coating. International journal of molecular sciences 15: 5263-5276.

144. Ferreira A, González G, González-Paz R, Feijoo J, Lira-Olivares J, et al. (2009) Bone collagen role in piezoelectric mediated remineralization. Acta Microscopica 18: 278-286.

145. Martin J, Schwartz Z, Hummert T, Schraub D, Simpson J, et al. (1995) Effect of titanium surface roughness on proliferation, differentiation, and protein synthesis of human osteoblast-like cells (MG63). Journal of biomedical materials research 29: 389-401.

146. Mendonça D, Miguez PA, Mendonça G, Yamauchi M, Aragão FJ, et al. (2011) Titanium surface topography affects collagen biosynthesis of adherent cells. Bone 49: 463-472.

147. Walter R, Kannan MB (2011) Influence of surface roughness on the corrosion behaviour of magnesium alloy. Materials & Design 32: 2350-2354.

148. Walter R, Kannan MB, He Y, Sandham A (2013) Effect of surface roughness on the in vitro degradation behaviour of a biodegradable magnesium-based alloy. Applied Surface Science 279: 343-348.

149. Huang H-H, Ho C-T, Lee T-H, Lee T-L, Liao K-K, et al. (2004) Effect of surface roughness of ground titanium on initial cell adhesion. Biomolecular engineering 21: 93-97.

150. Matschegewski C, Staehlke S, Loeffler R, Lange R, Chai F, et al. (2010) Cell architecture–cell function dependencies on titanium arrays with regular geometry. Biomaterials 31: 5729-5740.

151. Leikina E, Mertts M, Kuznetsova N, Leikin S (2002) Type I collagen is thermally unstable at body temperature. Proceedings of the National Academy of Sciences 99: 1314-1318.

152. Reznikov N, Almany-Magal R, Shahar R, Weiner S (2013) Three-dimensional imaging of collagen fibril organization in rat circumferential lamellar bone using a dual beam electron microscope reveals ordered and disordered sub-lamellar structures. Bone 52: 676-683.

153. Kadler KE, Hill A, Canty-Laird EG (2008) Collagen fibrillogenesis: fibronectin, integrins, and minor collagens as organizers and nucleators. Current opinion in cell biology 20: 495-501.

154. Drynda A, Seibt J, Hassel T, Bach FW, Peuster M (2013) Biocompatibility of fluoride-coated magnesium-calcium alloys with optimized degradation kinetics in a subcutaneous mouse model. Journal of Biomedical Materials Research Part A 101: 33-43.

155. Li N, Li Y, Wang Y, Li M, Cheng Y, et al. (2013) Corrosion resistance and cytotoxicity of a MgF2 coating on biomedical Mg–1Ca alloy via vacuum evaporation deposition method. Surface and Interface Analysis.

156. Lozano RM, Perez-Maceda BT, Carboneras M, Onofre-Bustamante E, Garcia-Alonso MC, et al. (2013) Response of MC3T3-E1 osteoblasts, L929 fibroblasts, and J774 macrophages to fluoride surface-modified AZ31 magnesium alloy. J Biomed Mater Res A 101: 2753-2762.

157. Yamamoto A, Terawaki T, Tsubakino H (2008) Microstructures and corrosion properties on fluoride treated magnesium alloy. Materials transactions 49: 1042-1047.

158. Jo J-H, Kang B-G, Shin K-S, Kim H-E, Hahn B-D, et al. (2011) Hydroxyapatite coating on magnesium with MgF2 interlayer for enhanced corrosion resistance and biocompatibility. Journal of Materials Science: Materials in Medicine 22: 2437-2447.

159. Seitz J-M, Eifler R, Stahl J, Kietzmann M, Bach F-W (2012) Characterization of MgNd2 alloy for potential applications in bioresorbable implantable devices. Acta Biomaterialia 8: 3852-3864.

160. Ao H, Xie Y, Tan H, Wu X, Liu G, et al. (2013) Improved hMSC functions on titanium coatings by type I collagen immobilization. J Biomed Mater Res A.

161. Sverzut AT, Crippa GE, Morra M, de Oliveira PT, Beloti MM, et al. (2012) Effects of type I collagen coating on titanium osseointegration: histomorphometric, cellular and molecular analyses. Biomed Mater 7: 035007.